

1 Shapes of magnetically controlled electron density structures in the dayside Martian ionosphere

2 C. Diéval<sup>1</sup>, A. J. Kopf<sup>2</sup> and J. A. Wild<sup>1</sup>.

3 <sup>1</sup>Department of Physics, Lancaster University, Lancaster, UK.

4 <sup>2</sup>Department of Physics and Astronomy, University of Iowa, Iowa City, IA, USA.

5 Corresponding author: cdieval05@gmail.com

6 Key points:

7 1. MARSIS AIS/Mars Express shows magnetically controlled density structures in the  
8 dayside Martian ionosphere.

9 2. Time series of electron density profiles corrected for dispersion are used to find the shape  
10 of 48 structures.

11 3. The majority of these structures are bulges, and a few are of other simple shapes: dip,  
12 downhill slope and uphill slope.

13

14 Abstract:

15 Non-horizontal localized electron density structures associated with regions of near radial  
16 crustal magnetic fields are routinely detected via radar oblique echoes on the dayside of Mars  
17 with the ionospheric sounding mode of the MARSIS radar onboard Mars Express. Previous  
18 studies mostly investigated these structures at a fixed plasma frequency and assumed that the  
19 larger apparent altitude of the structures compared to the normal surrounding ionosphere implied  
20 that they are bulges. However, the signal is subjected to dispersion when it propagates through

21 the plasma, so interpretations based on the apparent altitude should be treated with caution. We  
22 go further by investigating the frequency dependence (i.e. the altitude dependence) of the shape  
23 of 48 density structure events, using time series of MARSIS electron density profiles (EDPs)  
24 corrected for signal dispersion. Four possible simplest shapes are detected in these time series,  
25 which can give oblique echoes: bulges, dips, downhill slopes and uphill slopes. The altitude  
26 differences between the density structures and their edges are, in absolute value, larger at low  
27 frequency (high altitude) than at high frequency (low altitude), going from a few tens of km to a  
28 few km as frequency increases. Bulges dominate in numbers in most of the frequency range.  
29 Finally, the geographical extension of the density structures covers a wide range of crustal  
30 magnetic fields orientations, with near-vertical fields toward their center and near horizontal  
31 fields toward their edges, as expected. Transport processes are suggested to be a key driver for  
32 these density structures.

33

## 34 1) Introduction

35 The Martian upper atmosphere is not currently protected by a global magnetic dipole, and  
36 is therefore exposed to erosion by the incoming supersonic solar wind. An induced  
37 magnetosphere arises from the interaction between the conductive ionospheric obstacle and the  
38 solar wind plasma with its embedded interplanetary magnetic field (IMF) (e.g. Nagy et al.,  
39 2004). In addition, localized crustal magnetic fields (e.g. Acuña et al., 1999), remnants of a past  
40 Martian dynamo, are able to stand off the solar wind and locally control the magnetic topology at  
41 low altitudes in the forms of magnetic arcades with both footpoints anchored in the planetary  
42 crust (closed field lines), while in other areas the IMF is free to reach lower altitudes, imposing a

43 mostly horizontal induced magnetic field on the dayside (e.g. Brain et al., 2003). The magnetic  
44 anomalies form mini-magnetospheres which rotate with the planet, locally regulating  
45 atmospheric loss (e.g. Ramstad et al., 2016).

46         The Mars Advanced Radar for Subsurface and Ionospheric Sounding (MARSIS)  
47 experiment (Picardi et al., 2004) is part of the payload onboard the Mars Express (MEX) orbiter.  
48 MEX orbit has period 7.5 h and inclination  $\sim 86^\circ$  around Mars, with periapsis at  $\sim 300$  km and  
49 apoapsis at  $\sim 10000$  km. MARSIS is able to run in either a Sub-Surface mode or an Active  
50 Ionosphere Sounding mode. In the latter mode, which we are interested in here, the radar has  
51 provided numerous observations of the Martian ionosphere since August 2005 (e.g. Morgan et  
52 al., 2008; Němec et al., 2010; Sanchez-Cano et al., 2016). During topside sounding, a 40 m tip-  
53 to-tip dipole antenna sweeps through a frequency table (160 steps from 0.1 to 5.4 MHz, with  
54 resolution  $\Delta f/f \approx 2\%$ ) during 1.26 s by transmitting 91.4  $\mu\text{s}$  long sinusoidal pulses in a broad  
55 angular interval centered on nadir. The radio waves at a given frequency propagate, affected by  
56 dispersion (including varying group velocity and ray path bending), through the plasma layers of  
57 increasing plasma frequency until the local plasma frequency matches the pulse frequency, at  
58 which reflection occurs. Pulse reflection back to the radar nominally occurs at normal angle to  
59 the plasma layer. Two types of echoes can be detected at the same time: vertical echoes which  
60 reflect from the ionosphere below MEX (assumed to be ideally horizontally stratified) and  
61 oblique echoes which reflect from nearby non-horizontal density structures. The receiver  
62 measures the time delay for receiving the echo, in 80 bins of duration 91.4  $\mu\text{s}$  starting 253.9  $\mu\text{s}$   
63 and ending 7.56 ms after the start of the pulse. Full frequency sweeps are repeated at 7.54 s  
64 cadence. The basic measurement unit is a matrix of received power spectral density versus time  
65 delay and frequency, called an ionogram. In this mode, the topside sounder samples plasma

66 layers of increasing density as altitude decreases, from the spacecraft down to the ionospheric  
67 peak, according to the relationship  $f_p = 8980 \sqrt{N_e}$  between electron density  $N_e$  in  $\text{cm}^{-3}$  and  
68 plasma frequency  $f_p$  in Hz.

69 This study focusses on localized density structures associated with regions of near radial  
70 crustal magnetic fields, detected by MARSIS via oblique echoes, in the dayside Martian  
71 ionosphere (Andrews et al., 2014; Diéval et al., 2015; Duru et al., 2006; Gurnett et al., 2005;  
72 Nielsen et al., 2007a; Venkateswara Rao et al., 2017). When the spacecraft moves toward or  
73 away from such reflecting target, two echoes (one vertical and one oblique) are received, with  
74 the time separation between the echoes either decreasing or increasing. When the spacecraft  
75 passes directly over the structure, only one echo is detected; the echo may be vertical or oblique  
76 depending on the inclination of the plasma layer at each reflection point along the structure. This  
77 behavior is characterized by downward facing hyperbola signatures in echograms, which are  
78 displays of received intensity at a fixed frequency as function of time and echo range. In  
79 echograms, one can usually see that for a given frequency, the apex of the hyperbola appears to  
80 stand at or above the surrounding normal ionosphere (rms 19 km higher at a fixed frequency 1.8  
81 MHz according to Duru et al., 2006). The apparent altitude of the ionospheric echoes is  
82 calculated as the spacecraft altitude minus the echo range assuming speed of light in a vacuum.  
83 Gurnett et al. (2005) and Duru et al. (2006) exploited the higher apparent altitude of these  
84 structures to interpret them as bulges. Such plasma layers are inclined at a range of angles to the  
85 horizontal, up to  $90^\circ$  (Nielsen et al., 2007a). In addition, Venkateswara Rao et al. (2017) reported  
86 that the main ionospheric layer and the topside layers at higher altitude (topside layers  
87 discovered by Kopf et al., 2008, in the MARSIS data) may both cause oblique echoes in areas of

88 near radial crustal fields, indicating that the density contours of these topside layers can also be  
89 tilted.

90         The density structures have regularly been observed over periods of tens of days through  
91 subsequent MEX passes above the same magnetized areas, even though the upstream conditions  
92 were changing, indicating long term stability (Andrews et al., 2014). They occur above the  
93 strong magnetic anomalies of the Southern hemisphere as well as above the weak magnetic  
94 anomalies of the Northern hemisphere and their latitude extent matches rather well with the  
95 latitude extent of areas of near-radial fields of a given polarity (upward or downward oriented)  
96 (Diéval et al., 2015). It is therefore inferred that these structures are not single points, but are  
97 spatially extended and confined by the areas of magnetic cusps, reaching horizontal sizes of a  
98 few hundreds of km along the spacecraft footprint (Diéval et al., 2015). Oblique echoes are  
99 found in regions which have statistically low to moderate rates (20-50%) of open field lines  
100 (field lines with one footprint in the crust and the other connected to the IMF) (Diéval et al.,  
101 2015). This indicates that their regular occurrence does not depend on the infrequent magnetic  
102 reconnection between the crustal fields that rotate with the planet and the variable IMF. In  
103 addition, Diéval et al. (2015) reported simultaneous in situ observations of suprathermal electron  
104 distributions by the Electron Spectrometer (ELS) (Barabash et al., 2006) onboard MEX which  
105 indicated that the plasma regime (ionosphere or shocked solar wind) at the location of MEX  
106 (depending on the spacecraft position relative to plasma boundaries) had no influence on the  
107 observability of oblique echoes. Solar wind electron precipitation depends on the time-dependent  
108 magnetic reconnection between near-radial crustal fields and IMF to reach low altitudes along  
109 open field lines (which would otherwise be closed at other times, see e.g. Brain et al., 2007).

110           These recent results do not support the hypothesis proposed by earlier studies (Duru et  
111 al., 2006; Gurnett et al., 2005) that solar wind precipitation into magnetic cusps is the primary  
112 driver of these density structures. Gurnett et al. (2005) and Duru et al. (2006) had suggested that  
113 the solar wind penetrating to low altitude along open field lines would ionize and heat the  
114 neutrals, the latter causing an inflation of the neutral atmosphere (which moves additional EUV-  
115 ionizable material to higher altitude), such as to generate electron density bulges.

116           Other formation mechanisms have been proposed. If solar wind precipitation is involved,  
117 the resulting increase in electron temperature at the altitude of energy deposition causes a  
118 reduction of the ion-electron recombination rate, which increases the plasma density (Andrews et  
119 al., 2014). Another source of temperature increase may be Joule heating from field-aligned  
120 currents and Pedersen currents in regions of magnetic cusps (Fillingim et al., 2010, 2012;  
121 Rioussset et al., 2013, 2014; Withers et al., 2005). Finally, a 2-D ionospheric model taking plasma  
122 transport into account (Matta et al., 2015) has shown that an expanded ionosphere may form in  
123 regions of vertical crustal fields via upward diffusion, because it is easier for plasma to move  
124 along field lines than across them.

125           The previous studies of oblique echoes were carried out at a fixed frequency, though  
126 Nielsen et al. (2007a) reported that during simultaneous observations of vertical and oblique  
127 echoes, the maximum frequency of the oblique echo was often smaller than the maximum  
128 frequency of the vertical echo. This was interpreted as off-nadir reflections from density  
129 structures more tilted to the vertical at low frequencies than at high frequencies. However, there  
130 has been no systematic study of the frequency variation of the density structures so far. Since  
131 low frequencies correspond to high altitudes and high frequencies to low altitudes, the variations  
132 of these structures with altitude remain ambiguous. Also, it has been previously assumed that the

133 oblique echoes are reflected from bulges, because a given electron density level stands at a  
134 higher apparent altitude than the surrounding ionosphere. But, the apparent altitude estimation  
135 assumes that the pulse propagates at the speed of light in vacuum  $c$ , i.e. without correction for  
136 dispersion effects in the ionosphere. However, radio waves of frequency  $f$  will propagate with a  
137 group velocity  $V_g$  through an ionized medium of varying refractive index  $n = \sqrt{1 - \left(\frac{f_p}{f}\right)^2}$ . The  
138 group velocity  $V_g = c n = c \sqrt{1 - \left(\frac{f_p}{f}\right)^2}$  is less than the speed of light and becomes vanishingly  
139 small when  $f$  approaches  $f_p$ , at which signal reflection occurs. For a given time delay, the  
140 apparent range of the echo is therefore an upper limit for the real range. Correcting the altitude  
141 for dispersion confirms whether or not the density structures really stand higher than the  
142 surrounding ionosphere, and by how much.

143         The aim of the current work is to determine the correct shape and magnitude of the  
144 altitude changes across the structures as a function of frequency, and thus as a function of  
145 altitude, from the high densities near the ionospheric peak down to the lowest densities  
146 measurable by the topside sounding technique. This information may provide insight into the  
147 formation processes of the density structures.

148         The structure of the paper is as follows: the method is described in Section 2; the results  
149 are presented in Section 3 (divided into 3 subsections: A) Close look at individual events, B)  
150 Statistics, and C) Influence of crustal magnetic field orientation) and discussed in Section 4.  
151 Finally, we summarize in Section 5.

152

153 2) Method

154           Examples of hyperbola signatures from three density structures are shown in Figure 1.  
155   The time series runs from 13:00 to 13:15 Universal Time (UT) on 22 July 2006, orbit 3253.  
156   During the pass, MEX traveled above moderate strength magnetic anomalies from  $46^\circ$  to  $-9^\circ$   
157   latitude at a nearly fixed E. longitude of  $350^\circ$ , inbound toward periapsis (periapsis at 324 km  
158   altitude at 13:03:45 UT) and then outbound, on dayside. The altitude varied from 362 km to 709  
159   km and the solar zenith angle (SZA) varied from  $33^\circ$  to  $48^\circ$ . Panel (a) shows the crustal magnetic  
160   field model of Cain et al. (2003) evaluated at 150 km altitude at MEX footprint, with the  
161   magnetic zenith angle (left axis, black curve) and the magnetic field strength (right axis, red  
162   curve). The magnetic zenith angle is the angle of the magnetic field vector relative to the zenith:  
163    $0^\circ$  is vertical upward,  $90^\circ$  is horizontal. Panels (b), (c), (d) and (e) show MARSIS echograms at  
164   four frequencies: 1.52, 1.979, 2.548 and 3.03 MHz, equivalent to electron densities of  $2.86 \times 10^4$ ,  
165    $4.86 \times 10^4$ ,  $8.05 \times 10^4$  and  $1.14 \times 10^5 \text{ cm}^{-3}$ , at the reflection point, respectively. The vertical axis  
166   is the apparent altitude and the color codes the received intensity.

167           In all echograms, the vertical echo from the assumed ideally horizontally stratified  
168   ionosphere is identified as the bright yellow-red trace at near constant apparent altitude (varying  
169   from 100 down to 50 km as frequency increases). At frequency 1.52 and 1.979 MHz (panels b, c),  
170   three hyperbola signatures are visible, with apexes at 13:03:08, 13:08:39 and 13:12:03 UT. The  
171   signatures are marked with black ellipses. At 150 km altitude, the modeled field strength and  
172   magnetic zenith angle for these structures are: 109 nT and  $166^\circ$  at 13:03:08 UT, 194 nT and  $12^\circ$   
173   at 13:08:39 UT, and 48 nT and  $45^\circ$  at 13:12:03 UT (panel a). So these density structures are  
174   located in regions of near-vertical to oblique crustal fields, consistent with previous reports (e.g.  
175   Gurnett et al., 2005). We note that the oblique echoes tend to be more pronounced at low  
176   frequencies than at high frequencies. Indeed, there is only one hyperbola signature visible at



177 2.548 and 3.03 MHz (panels d, e). This indicates that the density contours are more inclined for  
178 low densities than for high densities, and therefore more able to give oblique echoes, in  
179 agreement with Nielsen et al. (2007a).

180 We have conducted a statistical study of a list of oblique echoes previously examined by  
181 Andrews et al. (2014) and Diéval et al. (2015). The original list from Andrews et al. (2014)  
182 contains 1126 events, detected when MEX was on dayside ( $SZA < 90^\circ$ ) with an altitude  $< 1100$   
183 km, spanning August 2005 to February 2013. The limit at 1100 km comes from the maximum  
184 range for which MARSIS can receive ionospheric reflections due to the time delay measurement  
185 window. The present study considers 1066 events from this list for which the hyperbola apexes  
186 stand at or above the surrounding ionosphere, as determined by Diéval et al. (2015). This ensures  
187 that we only look at density structures found directly below the spacecraft. We examine the  
188 density structures as a function of frequency (i.e. as a function of altitude); for convenience we  
189 need to look at all events in the same frequency bins, so we keep data starting from 1 October  
190 2005, after which the MARSIS frequency table became fixed: we keep 901 events from the  
191 previous list. It is convenient to work with frequencies here because the altitude of a plasma  
192 layer at a given frequency depends on many factors, including SZA, EUV intensity, strength and  
193 orientation of local magnetic field, distance of the planet from the Sun, etc..

194 The difference in apparent altitude between the hyperbola apexes and the normal  
195 surrounding ionosphere is usually positive and of the order of 19 km (e.g. Duru et al., 2006),  
196 which led to the assumption that the density structures are bulges. We want to check this  
197 assumption with the altitude measurement corrected for dispersion. The measured time delays  
198  $\Delta t(f)$  as a function of frequency can be inverted to obtain the frequency (and density) profile as  
199 a function of corrected altitude  $z(f_p)$ , referred to as the Electron Density Profile (EDP). The

200 Abel transformation gives the solution  $z(f_p) = \frac{2}{\pi} \int_{\alpha_0}^{\frac{\pi}{2}} c \Delta t(f_p \sin \alpha) d\alpha$  (Budden, 1961), where  
201  $\sin \alpha_0 = \frac{f_p(SC)}{f_p(max)}$ . The integration in frequency goes from the local plasma frequency at the  
202 spacecraft  $f_p(SC)$  to the maximum plasma frequency of the ionosphere  $f_p(max)$ .

203         There are several challenges associated to the detection of the ionospheric reflection at  
204 low frequencies, and thus to their inversion. The local plasma frequency is obtained from the  
205 MARSIS plasma oscillations excited in the antenna (e.g. Gurnett et al., 2005). These harmonics,  
206 recognizable as vertical bright stripes in MARSIS ionograms, make the estimation of reflection  
207 time delays more difficult at low frequencies. Electron cyclotron harmonics are also detected as  
208 horizontal bright stripes in MARSIS ionograms, when MARSIS is exposed to local magnetic  
209 fields of strength larger than a few tens of nT (Gurnett et al., 2005); these interferences again  
210 hinder the visibility of the ionospheric echo at low frequencies (the problem is even more acute  
211 above the magnetic anomalies, where we conduct the present work). Finally, the transmitted  
212 power falls off sharply at low frequencies, which makes the reflected signal often too low to be  
213 detectable at frequencies  $< \sim 1$  MHz (e.g. Morgan et al., 2013). These circumstances of low  
214 signal to noise ratio lead to a data gap between the local plasma frequency measured at MEX  
215 location and the lowest frequency measurable with the ionospheric reflection. The error on the  
216 determination of the corrected altitude becomes large if the frequency range of the gap is  
217 significant compared to the frequency range of the reflection (e.g. Morgan et al., 2013).

218         The density profiles presented here were obtained with the inversion method by Němec et  
219 al. (2016a), itself derived from the standard inversion method by Morgan et al. (2013). The  
220 inversion process in these methods assumes that the pulse propagates along the nadir direction  
221 (vertical echo), the ionosphere has plane parallel stratification, there are no magnetic effects, and

222 the density profile monotonically increases as altitude decreases. We note that the existence of  
223 non-monotonic density profiles presenting transient topside layers above the main density peak,  
224 for which the assumption of monotonic profiles is not valid (e.g. Kopf et al., 2008). Also, the  
225 plane parallel approximation breaks down near the terminator, where the plasma density is  
226 weaker and more variable than on dayside (e.g. Fox and Yeager, 2006; Gurnett et al., 2005). In  
227 addition, near the terminator, MARSIS sometimes detects ionospheric echoes and ground echoes  
228 overlapping for a range of frequencies, which can be explained by the strong horizontal density  
229 gradients present at the terminator (Duru et al., 2010). In this case, a single ionospheric reflection  
230 is observed, which is not vertical, but off-nadir. Finally, the lower densities near the terminator  
231 or at high spacecraft altitude increase the frequency range of the data gap compared to the  
232 measured frequency range of the ionospheric reflection, making the inversion process more  
233 error-prone.

234 For these reasons, Morgan et al. (2013) considered EDPs as unreliable for  $SZA > 85^\circ$  or  
235 spacecraft altitude  $> 800$  km. In practice, this means that they rejected profiles for which the  
236 frequency range of the gap is larger than the frequency range of the ionospheric echo and/or  
237 larger than 1 MHz. In addition, Morgan et al. (2013) have excluded profiles with ionospheric  
238 peak frequencies between 2.25 and 2.3 MHz, for which there is a sensitivity gap. Since the  
239 terminator region causes many difficulties, we restrict our study to  $SZA < 85^\circ$ : this leaves 890  
240 events to study. The major difference between the two mentioned inversion methods is the  
241 functional form used for  $f_p(z)$  in the low frequency data gap. The reader is directed to Němec et  
242 al. (2016a) for details.

243 Finally one may question whether the assumptions of vertical reflection and plane  
244 parallel stratification are reasonable in regions of density structures (with inclined density

245 layers). We discuss the problem and make a check of these assumptions in appendix A. The  
246 conclusion of this check is that for the events investigated in this work, the assumption of plane  
247 parallel stratification is definitively good, and the assumption of vertical propagation is good  
248 enough to use as an approximation. Therefore we trust these EDPs are appropriate for this study.

249 We want to look at time series of EDPs for each density structure, by selecting all  
250 available EDPs (from the processing by Morgan et al., 2013) during the period for which the  
251 spacecraft passes overhead the structure. For this purpose, we need the echograms, which we  
252 integrate over a range of frequencies typical for oblique echoes (we chose between 1.8 and 2  
253 MHz), rather than just taking one frequency level, because it improves the noise/ratio of the  
254 echogram (less background noise and more pronounced ionospheric traces, resulting from  
255 combining different frequencies) and shows ionospheric features which could possibly be missed  
256 if using only one frequency level. This period of overhead pass is estimated from the MARSIS  
257 echograms by considering the time at which the hyperbola signature starts merging and then  
258 stops merging with the main surrounding ionosphere echo. This exercise is a rough estimate (but  
259 good enough for our purpose) because of the following difficulties. 1) The merging time for each  
260 hyperbola leg can take the duration of several ionograms (several times 7.54 s), and is thus not  
261 instantaneous or easy to determine. 2) Several structures can be superposed on top of each other  
262 due to the frequent occurrence of oblique echoes in neighboring regions of alternating radial field  
263 polarities; this makes it difficult to separate individual structures. 3) The structure can present  
264 only one clear leg or present one or two short/unclear legs, which make it hard to determine  
265 where are the edges of the structure. 4) In practice, the period of overhead pass is itself limited  
266 by the coverage of available EDPs during this period. From the previous list, there are 165 events  
267 for which there are at least 3 available EDPs to make a time series. Figure 2 shows the state of

268 the EDP coverage for these 165 events. Panel (a) shows the distribution of the duration of events  
269 for all the events as estimated from the procedure above (panel a), which is broad with a tail at  
270 high values, median of 90 seconds, and minimum and maximum values of 30 and 242 seconds  
271 respectively. Such durations of one to several minutes are consistent with the previous report by  
272 Diéval et al. (2015). Panel (b) shows the restrictions from the processing by Morgan et al. (2013)  
273 is such that there are not always as many EDPs available as one would wish for a complete  
274 coverage of each event. The distribution of the number of available EDPs divided by the number  
275 of ionograms during the duration of each event (i.e. ratio of numbers), for all the events, is broad  
276 with a median of 0.58 and minimum and maximum values of 0.12 and 1 respectively.

277 It is preferable not only to have a good proportion of EDPs available (to reduce the data  
278 gaps) but also to have the first and last available EDPs covering as close to the beginning and  
279 end (edges) of the overhead pass as possible. Panel (c) shows the distribution of the duration of  
280 the EDP coverage divided by the event duration for each event (i.e. ratio of durations), for all the  
281 events, peaking at high values, with a median of 0.85 and minimum and maximum values of 0.14  
282 and 1 respectively; so a majority of events has available EDPs rather close to the edges of the  
283 structure, which is a good sign. Panel (d) shows a scatter plot of the ratio of durations plotted  
284 versus the ratio of numbers, colored by the number of available EDPs for the duration of each  
285 event, for all the events. Naturally, the number of available EDPs increases as both ratios  
286 increase. We decide to keep 48 events for which the number of available EDPs divided by the  
287 number of ionograms is  $\geq 0.7$  and for which the duration of the EDP coverage divided by the  
288 event duration is  $\geq 0.7$ . For these 48 events we are confident we have a reasonable EDP  
289 coverage, and therefore a reasonable determination of the shape of the time series of EDPs. The

290 minimum and maximum values of the number of available EDPs per event become 4 and 20  
291 respectively.

292 We will compare the altitude variations for the EDPs of the time series for each event, at  
293 a fixed sounding frequency, for all frequencies for which ionospheric traces were detected (the  
294 local frequency is excluded from analysis). To make it easier to identify the shapes of density  
295 structures, we visually inspect these time series at a few selected frequencies typical for the  
296 detection of oblique echoes, to select one EDP which defines best the simplest shape of the time  
297 series, in comparison with the first and last EDPs (beginning and end edges) of the time series  
298 (i.e. using three EDPs to find the simplest shape). This selected EDP is thus a reference profile to  
299 which we compare the other EDPs in the time series, and is referred to as “point of interest” PI  
300 EDP. By choosing the PI EDP in this manner, we do not require the PI EDP to sit at the center of  
301 the time series nor at the apex of the hyperbola signature (so there can be unequal numbers of  
302 EDPs on either sides of the PI EDP). The determination of the PI EDP is somehow subjective,  
303 especially if the shape of the time series is complicated, with complex variations; in addition the  
304 shape can change with increasing frequency, although gradually. Anyway this exercise is made  
305 for helping identify the altitude variations relative to a reference EDP.

306 At a fixed frequency, the 4 simplest possible shapes are as follows. 1) If the altitude of  
307 the PI EDP is higher than the altitude of both beginning and end EDPs, then we call the shape  
308 “bulge”. In this case, there is first an increase and then a decrease of the altitude level, the PI  
309 EDP having the highest altitude in the time series. 2) If the altitude of the PI EDP is lower than  
310 the altitude of both beginning and end EDPs, then we call the shape “dip”. In this case there is  
311 first a decrease then an increase in altitude, the PI EDP having the lowest altitude in the time  
312 series. 3) If the altitude of the PI EDP is higher than the altitude of the beginning EDP and lower

313 than the altitude of the end EDP, then we call the shape “uphill slope”. 4) If the altitude of the PI  
314 EDP is lower than the altitude of the beginning EDP and higher than the altitude of the end EDP,  
315 then we call the shape “downhill slope”. The PI EDP for an uphill slope or downhill slope is  
316 determined visually from the EDP bringing a change of slope along the time series, i.e. this EDP  
317 can be used to test if the slope is convex or concave. The four possible simplest shapes  
318 mentioned: bulge, dip, uphill slope and downhill slope, have been found in the 48 events we  
319 have examined, as we will see below.

320 In the following figures, for a given event, we either use the altitude differences between  
321 the PI EDP and all other EDPs in the time series for a detailed study, or we use the altitude  
322 differences between the PI EDP and the beginning or end EDPs (edges) for a more concise  
323 study. Several times we will work at a fixed frequency 1.936 MHz, for illustration of a typical  
324 frequency at which oblique echoes are detected. We note that the uncertainty on the range of the  
325 ionospheric echo corresponds to one pixel and is given by  $c \times \Delta t / 2 = 13.7 \text{ km} = \pm 6.9 \text{ km}$ . For  
326 this work, it means that, for an event at a fixed frequency, if the absolute value of the altitude  
327 difference between the PI EDP and another EDP of the time series is larger (smaller) than 13.7  
328 km, then this altitude difference is resolved (unresolved) by the measurement.

329

### 330 3) Results

#### 331 A) Close look at individual events

332 In this subsection, we investigate the detailed variations of a few events as a function of  
333 frequency and time. Figure 3 shows time series in 4 columns corresponding each to one example  
334 of event with a rather clear shape in EDP time series at different frequency levels (see top row):

335 (a) bulge, (b) downhill, (c) dip and (d) uphill. The date and time of PI EDP for each event are  
336 indicated in the figure. In all panels, the vertical dashed lines mark particular measurement times:  
337 PI EDP (magenta), beginning and end EDPs (black), beginning and end times determined from  
338 the echogram (green). The top row shows time series of EDPs color coded for 6 selected  
339 frequencies between 1.433 and 2.505 MHz. Our working frequency of 1.936 MHz lies between  
340 the green and magenta curves.

341 We see that bulges are indeed detected, consistent with expectations from using the  
342 uncorrected apparent altitude (e.g. Duru et al., 2006). Interestingly, other shapes are also  
343 detected: dips (as proposed by Nielsen et al., 2007a), uphill and downhill slopes; in principle  
344 their inclined density contour levels are able to give oblique echoes. We see sometimes complex  
345 altitude variations which tend to complicate the shape of events, but the simplest shapes were  
346 rather easy to determine for these 4 cases. For example, the dip event in column (c) appears more  
347 clearly as a dip if one considers the gradual decrease and then gradual increase of altitude on  
348 either side of the PI EDP, with the gradual decrease being shortly interrupted by an amplitude  
349 quirk. As we see already here, and will see again later, that the altitude variations tend to be  
350 larger at low frequency (high altitude) than at high frequency (low altitude), and the shape can  
351 remain the same at all frequencies or change with frequency.

352 The second row of Figure 3 shows the time series of altitude differences between the PI  
353 EDP and the other EDPs of the time series for these 4 events, at a fixed frequency 1.936 MHz.  
354 Positive values mean that the PI EDP stands at higher altitude than these EDPs, negative values  
355 mean that the PI EDP stands at lower altitude than these EDPs, zero values correspond to the PI  
356 EDP or any EDP with identical altitude. For clarity, the magenta vertical dashed line indicates  
357 the position of the PI EDP. At frequency 1.936 MHz, there are 33 events out of 48 classified as



358 bulges, 6 as dips, 4 as downhill slopes, 3 as uphill slopes, and 2 undetermined (data gap). As we  
359 will see later, at this frequency the bulges dominate the number of events, compared to other  
360 shapes. Interestingly, this result, based on altitude profiles corrected for dispersion, confirms the  
361 insights of Gurnett et al. (2005) and Duru et al. (2006) based on the apparent altitudes  
362 uncorrected for dispersion.

363         In the bottom row of Figure 3, we inspect the hyperbola signatures in the echograms  
364 integrated for 1.8-2 MHz for these 4 events. These panels have an extended time range to give a  
365 better view of the oblique echoes caused by the density structures. While the hyperbola signature  
366 in column (a) presents two clear legs (here there is a bulge), the hyperbola signature in the other  
367 columns have only one clear leg, with the leg at the beginning of the signature for column (c)  
368 (here there is a dip) or the leg at the end of the signature for columns (b) and (d) (here there are  
369 downhill and uphill slopes respectively). We also see that the point of highest apparent altitude  
370 on the hyperbola signature does not necessarily correspond to the highest (or even lowest)  
371 altitude point (for bulges and dips) in the time series of corrected altitudes from the top row.  
372 Examination of the other events in the list suggests two points. 1) The variations of the apparent  
373 altitude of the hyperbola signature on the echogram bear no predictable relation to the variations  
374 of the corrected altitudes in the same frequency range. 2) The presence of two clear hyperbola  
375 legs or only one clear leg at the beginning or end of the structure cannot be reliably related to the  
376 simplest shape of structures in the same frequency range. One could have expected, from  
377 considerations of spacecraft motion moving toward and then away from a structure, that the  
378 slopes on either side of a bulge or dip should cause 2 clear legs at the beginning and end of the  
379 structure, while an uphill slope would cause just one clear leg at the beginning of the structure  
380 and a downhill slope would cause just one clear leg at the end of the structure. It is likely that the

381 key to understand these two issues arises from both the signal dispersion (including varying  
382 group velocity and ray path bending as the plasma frequency of the medium changes during their  
383 propagation) and the likely complicated geometry of the ray paths related to the presence of  
384 horizontal density gradients (possible multiple reflections for a given ray). Ray tracing through  
385 models of ionospheric layers obtained from the MARSIS measurements, taking signal dispersion  
386 into account, would be illuminating to solve these two issues, although it is beyond the scope of  
387 the present work.

388         In Figure 4 we check the EDPs for their full frequency range for the same 4 events.  
389 Figure 4 displays the series of EDPs for each event into four panels: bulge (a), downhill slope  
390 (b), dip (c) and uphill slope (d). For each event, the red curve is the PI EDP, the black curves are  
391 the other EDPs for the time series, the colored dots mark the same data points (color coded with  
392 frequency) as in Figure 3. For each event, the EDPs are plotted versus  $\log_{10}(\text{density})$  in  $\text{cm}^{-3}$  and  
393 the densities of the successive EDPs are multiplied by  $10^0$ ,  $10^1$ ,  $10^2$ , etc., for clarity. Because this  
394 way of displaying EDPs is equivalent to a time series of EDPs, one can see that for each event,  
395 the shapes of the color coded altitude variations at the various frequencies follow the same  
396 shapes as in Figure 3. We remark for these 4 events (noticed also for the other events in the list)  
397 that the altitude range of these EDPs actually shifts down or up in altitude to follow the shape in  
398 the time series of EDPs from Figure 3; the ionospheric peak altitude tends to follow this trend  
399 too. For example, for the bulge event the altitude range of each EDP shifts upward until the PI  
400 EDP is reached, then the altitude range of the following EDPs shifts down, like the entire topside  
401 ionosphere moves up then down in altitude. Similarly, the entire topside ionosphere appears to  
402 continuously move up for the uphill event, continuously move down for the downhill event and  
403 first move down then move up for the dip event. We note that the absolute value of the

404 difference in SZA between the first and last EDPs of the time series for each event is typically  
405 small, with a median of  $1.6^\circ$ , thus these altitude changes are independent of the SZA.

406         When examining the EDPs for the overall of events of the list, there are sometimes hints  
407 of vertical gradients in the form of slight ledges, for example at 220 km altitude for the 5<sup>th</sup> EDP  
408 from the left in panel (d). These vertical gradients may be density bite-outs, density bumps and  
409 topside layers (e.g. Kopf et al., 2008, Withers et al., 2005) which would have been attenuated in  
410 the EDPs because of two reasons. 1) When there is a non-monotonic variation in the electron  
411 density (i.e. a valley: decrease in density as altitude decreases above the main peak), MARSIS  
412 cannot observe this valley directly because low frequency signals get reflected at layers of larger  
413 plasma frequency present at higher altitudes above the valley, although indirect observations are  
414 possible (e.g. Wang et al., 2009), 2) the processing of the EDPs by Morgan et al. (2013) assumes  
415 monotonic profiles.

416         We examine the trends of ionospheric peak altitude and peak frequency for the same 4  
417 events in Figure 5, which is organized as columns: (a) bulge, (b) downhill slope, (c) dip, (d)  
418 uphill slope. The first row has almost the same format as the first row of Figure 3. The second  
419 and the third row show time series of peak frequency and peak altitude, respectively. For these  
420 events, the variation of the peak frequency presents no clear relationship compared to the  
421 variation of the altitude levels at a few lower frequencies: although the peak frequency tends to  
422 increase during the bulge event, the peak frequency just increases during the downhill slope  
423 event, also just increases during the dip event and stays constant during the uphill event. From  
424 looking at the rest of the events in the list, there is no systematic increase (or decrease) in peak  
425 density in the regions giving oblique echoes. We note that individual cases of high peak densities  
426 in areas of strong near vertical crustal fields were reported by e.g. Nielsen et al. (2007b). On the

427 other end, the evolution of the peak altitude for the 4 events tends to follow the variations of  
428 altitude levels at lower frequencies, such as to track the shape of the time series of EDPs. This  
429 trend was observed as well for the rest of the events in the list.

430 Finally, the evolution of the simplest shape of events with frequency is also examined for  
431 the full frequency range of a few selected events. Figure 6 shows the shape classification of 6  
432 events as function of frequency, displayed as colored dots: bulge (red), concave slope (green),  
433 convex slope (blue) and dip (black). Here we use the altitude differences between the PI EDP  
434 and the first or last EDP of the time series, at a fixed frequency, for every frequency of each  
435 event. It is useful to consider the convex or concave nature of a slope here, because a convex  
436 slope swells downward (looks like a dip) and a concave slope swells upward (looks like a bulge).  
437 For a given slope event, at a fixed frequency, the event is determined as convex (concave) if the  
438 second derivative of the altitude from the time series of three EDPs is positive (negative). The  
439 date and time of the PI EDPs are indicated in each panel. In panels (e) and (f), the event remains  
440 with the same shape at all frequencies: bulge and dip, respectively. In panel (a), the event  
441 evolves from concave, to bulge then to concave, as frequency increases. In panel (c), the event  
442 evolves from convex, to concave, then to bulge. In panel (b), the event evolves from concave, to  
443 convex, to dip, to convex, and then to concave. In panel (d), the event evolves from concave, to  
444 bulge, to concave, to convex, and then to concave.

445 It is observed that the shape change is gradual such that there are always concave and  
446 convex slopes in the correct order to separate bulges and dips; this is natural since a concave  
447 slope looks like a bulge and a convex slope looks like a dip. This is confirmed by examining the  
448 other events in the list. We see that in the case of events changing shape over frequency: if the  
449 shape is not a bulge in a given segment of the frequency range, there is no marked preference for

450 observing dips rather than convex slopes or concave slopes. This holds for the entire frequency  
451 range. Note that the shape of an individual event at a fixed frequency may be uncertain if the  
452 altitude differences are unresolved, i.e., in absolute value are lower, than the 13.7 km range  
453 resolution (this is the case for many events as we will see later). Despite this, there is a  
454 systematic gradual transition over frequency. This result validates the determination of shape  
455 over frequency for individual events, whatever the magnitude of the altitude differences.

456

## 457 B) Statistics

458 Now we consider all the events for statistics purposes. We start with inspecting the  
459 magnitude of the altitude differences for all the events as a function of frequency for the entire  
460 frequency range. Figure 7 shows in panels (a, b) the altitude differences between the PI EDP and  
461 the edge EDP of each event, versus frequency, for all the events, and similarly, in panels (c, d),  
462 the altitude differences between the PI EDP and the edge EDP relative to the altitude of the PI  
463 EDP of each event. The edge EDP is either the first or last EDP of the time series of a given  
464 event. Altitude differences which change sign over frequency are plotted in panel (b, d), while  
465 altitude differences keeping the same sign over frequency are plotted in panel (a, c). Median  
466 values of the altitude differences over frequency are indicated by red dots. The median values of  
467 the altitude differences being all positive or all negative over frequency are treated separately.  
468 Horizontal black dashed lines delimitate regions where the absolute values of altitude differences  
469 are  $>$  or  $<$  13.7 km (13.7 km is the range resolution). Colored patches in panels (a,b) help  
470 distinguishing these regions of resolved or unresolved altitude differences (cyan or white).

471 In panels (a, c), the altitude differences tend to be larger in absolute value at low  
472 frequency than at high frequency, both for all-negative and all-positive differences. These trends  
473 are also reproduced by the medians values. The largest values of altitude differences (several  
474 tens of kilometers or several tens of % relative to the PI EDP) are found at low frequencies, and  
475 the lowest values (several kilometers or several % relative to the PI EDP) at high frequencies.  
476 Thus, it is more likely for the altitude differences to be unresolved ( $< 13.7$  km) at high  
477 frequencies (low altitudes) than at low frequencies (high altitudes). The absolute value of the  
478 median of altitude differences becomes larger than 13.7 km at a fixed frequency of 1.848 MHz  
479 (1.805 MHz) for the all-negative (all-positive) altitude differences. Finally, a majority of altitude  
480 differences lie completely within the unresolved region (cyan patch). Similarly, for the altitude  
481 differences changing sign over frequency (panels b, d), the altitude differences tend to be larger  
482 in absolute value at low frequency than at high frequency. These trends are also reproduced by  
483 the medians values. The contribution of both negative and positive values at each frequency  
484 contributes to decrease the absolute value of the median, to be below 13.7 km. The results are  
485 consistent with the finding by Nielsen et al. (2007a) of density contours being more tilted at low  
486 frequencies than at high frequencies.

487 In Figure 8, we check the distributions of altitude differences between the PI EDP and the  
488 edge EDP, for all the events, separated between the 4 simplest shapes, at 4 different frequencies  
489 corresponding to 4 panels: (a) 1.411, (b) 1.848, (c) 2.155 and (d) 2.854 MHz. In each panel, the  
490 distributions are color coded per shape and plotted as stacked bars on top of each other in every  
491 bin: bulge (red), black (dip), downhill slope (green) and uphill slope (blue). Regions of  
492  $\text{abs}(\text{altitude differences}) < \text{or} > 13.7$  km are delimited by thin vertical black dashed lines and  
493 colored patches (unresolved: cyan, resolved: white). For bulges, both sides of the structure has

494 positive values of altitude differences; similarly for dips both sides have negative values of  
495 altitude differences; for uphill slopes the value of altitude difference is positive for the first EDP  
496 and negative for the last EDP; for downhill slopes the value of altitude difference is negative for  
497 the first EDP and positive for the last EDP. At the 4 frequencies shown, the number of bulges  
498 dominates the number of other shapes (we will see this also later). As frequency increases, the  
499 spread of altitude difference values tends to decrease for each shape, with less extreme values  
500 present, such that the distributions become more confined within the region of  $\text{abs}(\text{altitude}$   
501  $\text{differences}) < 13.7 \text{ km}$  (cyan). At a fixed frequency, the absolute value of the altitude differences  
502 tends to be larger for bulges than for other shapes, and tends to be larger at low frequency than at  
503 high frequency for bulges but less evident for other shapes (see also the median values for the 4  
504 distributions of simplest shapes indicated as color coded text in each panel). There may be an  
505 effect of the number of events regarding the trends of bulges versus other shapes, since there are  
506 far more bulges than other shapes, as we will see later. For illustration, the median value of 12.4  
507 km for the altitude differences in bulges at a fixed frequency 1.848 MHz is of the same order as  
508 the rms apparent altitude difference between the hyperbola apex and the main ionosphere of 19  
509 km at a fixed frequency 1.8 MHz determined by Duru et al. (2006).

510 We also examine, in Figure 9, the distribution of the four simplest shapes of all events in  
511 the entire frequency range, displayed as color coded symbols: bulges (red dots), dips (black  
512 diamonds), downhill slopes (green '+'), uphill slopes (blue 'x'). The number of events drops  
513 sharply at frequencies below 1 MHz because of the various issues of signal to noise ratio  
514 mentioned earlier, and drops sharply at frequencies above 3 MHz ( $1.1 \times 10^5 \text{ cm}^{-3}$ ) because the  
515 ionospheric echo is constrained by the peak density (which varies between  $0.5$  and  $1.5 \times 10^5 \text{ cm}^{-3}$   
516 on dayside, see e.g. Morgan et al., 2008). The distribution of bulges dominates the total number

517 of events and peaks at 2.111 MHz with 36 events; at the same frequency there are 5 downhill  
518 slope events, 1 uphill slope event and 5 dips. The distribution of uphill slope events peaks with 5  
519 events at 7 different frequencies those highest is 1.63 MHz, for downhill slope events it peaks  
520 with 7 events at 3 frequencies those highest is 1.455 MHz and for dips it peaks with 8 events at 7  
521 different frequencies those highest is 1.52 MHz. Thus, the number of bulges peaks at a much  
522 higher frequency than the numbers of other shapes does. For frequencies below 0.951 MHz all  
523 shapes have comparably small numbers of events. This is likely an effect of bad statistics, since  
524 there are challenges for measuring the ionospheric trace at frequencies  $< 1$  MHz. For higher  
525 frequencies the number of bulges is much larger than the other numbers. It is worthwhile to note  
526 that for the 48 events, there are 20 events detected during MEX passes going from North to  
527 South, and 28 events detected during passes going from South to North; still the proportions of  
528 uphill and downhill slope events remain similar in both instances, as expected.

529 Finally, we can compare the behaviors of the ionospheric peak altitudes and peak  
530 frequencies to the behavior of the altitude level at 1.936 MHz, for all the events, to check the  
531 case studies trends from Figure 5. Then, Figure 10 shows scatter plots of the altitude level at  
532 1.936 MHz versus the peak frequency (panel a) and versus the peak altitude (panel b), both using  
533 all the available EDPs in the time series of all the events. As suggested from the inspection of  
534 individual events, we see that when the selected altitude level increases, the peak frequency has a  
535 weak trend of increase (broad scatter), while the peak altitude has a clear trend of increase  
536 (narrow scatter). We confirm that these trends remain visible (especially for the peak altitude)  
537 when separating the events into the 4 types of simplest shapes at 1.936 MHz (not shown). For the  
538 case of bulges (the majority of events), the peak altitude has a marked tendency of a local



539 increase and the peak frequency has a less evident tendency of a local increase, in areas of  
540 oblique echoes.

541

### 542 C) Influence of crustal magnetic field orientation

543 Previous studies have shown the close association between oblique echoes and near-  
544 vertical crustal magnetic fields (e.g. Gurnett et al., 2005). Here we inspect the relationships of the  
545 altitude differences in areas of oblique echoes and corresponding magnetic anomalies, first for a  
546 few individual events, then for all the events. We use the Cain et al. (2003) crustal magnetic field  
547 model evaluated at 150 km altitude at MEX footprint.

548 Figure 11 shows maps of two regions of magnetic anomalies of moderate strength near  
549 the equator, in the Southern hemisphere (panel a) and Northern hemisphere (panel b). Selected  
550 contours of the angle of the crustal magnetic field to the vertical are displayed using the left side  
551 colormap. The horizontal orientation is  $0^\circ$  and the vertical orientation is  $90^\circ$ . Field strengths  $< 30$   
552 nT are ignored. The footprints of MEX location at the times of available EDPs for individual  
553 events detected in these regions are superposed onto the maps. The location of the PI EDP is  
554 marked by a black 'x' for each event and its date and time written in the panels. The events are  
555 each colored with the altitude differences between the PI EDP and the other EDPs of the time  
556 series relative to the altitude of the PI EDP (in %), all taken at a fixed frequency 1.936 MHz.  
557 Negative values mean that the PI EDP stands at altitudes below these EDPs, zero values mean  
558 that the PI EDP stands at the same altitude as these EDPs (the PI EDP itself or other EDPs of  
559 equal altitude), and positive values mean that the PI EDP stands at altitudes above these EDPs.

560 Negative values are in blue, zero values in white and positive values in red, using the colormap  
561 on the right side.

562 In both maps, there are events detected geographically close to each other, at different  
563 dates and times, with similar shapes or different shapes, from their altitude differences. Thus the  
564 shape may vary in geographical location and time. The range of crustal field orientations,  
565 through the latitudinal extension of the events (MEX orbits are nearly fixed in longitude near the  
566 equator), covers well the areas of near radial field near the center of the events, and the areas of  
567 near horizontal field near their edges. The time of the PI EDP is determined from the timeseries  
568 of EDPs, and is not necessarily associated to near vertical fields.

569 Finally, we check whether the magnitude and the sign of the altitude variations at a fixed  
570 frequency 1.936 MHz are affected by the crustal field orientation, for all the available EDPs of  
571 the time series of all the events, in Figure 12. The data points of the altitude differences between  
572 the PI EDP and itself (which are zero values) are removed from this figure, so the zero values  
573 which remain are only due to other EDPs with altitudes identical to the PI EDP. Panel (a)  
574 displays the distribution of the angle of the crustal field to the vertical, which covers the full  
575 range of possible angles (minimum and maximum are 2.5 and 89.5°), with 25<sup>th</sup>, 50<sup>th</sup> and 75<sup>th</sup>  
576 percentiles of 26.6, 42.0 and 61.8°, respectively. The distribution peaks at angles closer to the  
577 vertical than to the horizontal (it peaks at angles < 45°). This is expected because the density  
578 structures giving oblique echoes are usually found in areas of vertical to oblique crustal field  
579 orientation, with a latitude extension covering the latitude extension of the magnetic cusps, the  
580 magnetic field strength being not important (e.g. Duru et al., 2006, Diéval et al., 2015). The time  
581 series of EDPs cover whenever possible up to the edges of the density structures as determined

582 from the echograms, thus angles closer to the horizontal are also sampled, particularly near the  
583 edges.

584 Panel (b) shows the distribution of the altitude differences between the PI EDP and the  
585 other EDPs of the time series, which presents negative and positive values (minimum and  
586 maximum are -24.7 and 44.1 km), peaks at positive values (there is a majority of bulges which  
587 contribute positive altitude differences), with 25<sup>th</sup>, 50<sup>th</sup> and 75<sup>th</sup> percentiles of 1.1, 5.8 and 12.3  
588 km, respectively. There are 390 data points, whose 309 are positive differences and 76 are  
589 negative ones. In absolute value, typically, the smallest altitude differences are found close to the  
590 PI EDP, and the largest values close to the edges of the structure. Panel (c) shows the distribution  
591 of altitude differences between the PI EDP and the other EDPs of the time series, relative to the  
592 altitude of the PI EDP (in %), which shows similar behavior to the former distribution. It  
593 presents negative and positive values (-13.5 and 21.2 %, respectively), peaks at positive values,  
594 with 25<sup>th</sup>, 50<sup>th</sup> and 75<sup>th</sup> percentiles of 0.6, 2.9 and 6.4 %, respectively.

595 Panel (d) displays a superposed epoch analysis of the angle of the crustal field to the  
596 vertical, using the time difference in seconds between the available EDP in the time series and  
597 the center time of the density structure (positive values are after and negative values are before  
598 the center time, respectively). For each event, the center time is the time at the center of the  
599 interval bounded by the edges of the structure as determined from the echogram. A red line  
600 indicates the median values of angles as a function of superposed epoch time. The distribution  
601 varies like a broad “v” shape, as well as the median values. We have checked that individual  
602 time series often vary such as to be centered near a “v” shape. The crustal field orientation  
603 changes from more vertical to more horizontal, as one progress from the center of the structures  
604 toward their beginning and end edges. This trend is expected, since the latitudinal extension of

605 the structures giving oblique echoes tends to cover the latitudinal extension of the corresponding  
606 magnetic cusps (e.g. Diéval et al., 2015).

607 Panel (e) displays a superposed epoch analysis of the relative altitude differences, using  
608 the time difference in seconds between the available EDP in the time series and the PI EDP  
609 (positive values are after and negative values are before the PI EDP, respectively). A red line  
610 indicates the median of the relative altitude differences as a function of superposed epoch time.  
611 When considering the majority of points being positive, the distribution varies like a broad “v”  
612 shape. We have checked that individual profiles plotted in this way do not necessarily exhibit a  
613 clear “v” shape (even when including only bulges), because of the ample fluctuations existing in  
614 the time series. The median values also vary as a “v” shape. Since the majority of density  
615 structures are bulges, this means that the altitude level at a fixed frequency tends to stand further  
616 down (relative to the PI EDP) as one progresses toward both beginning and end edges of the  
617 structures.

618 Panel (f) shows a scatter plot of the angle of the crustal field angle to the vertical versus  
619 the relative altitude differences. There is no obvious trend here, with an extended range of  
620 altitude differences (both for positive and negative ones) whatever the crustal field orientation.  
621 Considering the events of the 4 simplest shapes separately does not affect this result (not shown).  
622 There is however a slight trend to find the largest positive values toward large angles, i.e. to find  
623 the edges of the density structures (mostly bulges) near the edges of magnetic cusps (near  
624 horizontal field orientation).

625

626 4) Discussion

627 We have examined the behavior of the density structures from the lowest measurable  
628 densities down to the densities approaching the ionospheric peak. The absolute value of the  
629 median of altitude differences becomes larger than 13.7 km at a fixed frequency of 1.848 MHz  
630 (1.805 MHz) for the all-negative (all-positive) altitude differences between the PI EDP and the  
631 edge EDPs; we take the typical transition frequency as the average between these 2 values: 1.826  
632 MHz, corresponding to  $4.13 \times 10^4 \text{ cm}^{-3}$ . This threshold is marked with a vertical red dashed line  
633 in Figure 7a.

634 It is important to note that the ionosphere has several regimes depending on altitude. At  
635 low altitude near the ionospheric peak (near 125 km altitude at  $\text{SZA}=0^\circ$ ) the plasma is in  
636 photochemical equilibrium (electron production rate balances recombination); for ions the  
637 transport time is much longer than the chemical loss time. At high altitude the chemical loss time  
638 becomes much longer than the transport time because of the reduced densities, the ions are then  
639 transported over significant distances before they are lost to chemical reactions: the ionosphere is  
640 in the transport regime (above 200 km altitude). We can check the altitude range for the behavior  
641 of the density structures and compare it to these regimes. For this purpose, we use the empirical  
642 model of the Martian dayside ionosphere by Němec et al. (2011a; 2016b), based on MARSIS  
643 AIS EDPs, which incorporates dependencies on the solar radio flux F10.7, the Sun-Mars distance  
644 R and the strength of the crustal magnetic field B at 400 km altitude (see  
645 <http://aurora.troja.mff.cuni.cz/nemec/n11/>). We take average conditions since the list of events  
646 covers different periods over several Martian years and we use conditions of moderate magnetic  
647 anomalies:  $\text{F10.7}=90 \text{ sfu}$ ,  $\text{R}=1.5 \text{ AU}$  and  $\text{B}=30 \text{ nT}$ .

648 The altitude of the level  $4.13 \times 10^4 \text{ cm}^{-3}$  (1.826 MHz) varies from 198 km at  $\text{SZA}=0^\circ$  to  
649 188 km at  $\text{SZA}=85^\circ$ . Therefore there is a transition altitude of  $\sim 190 - 200 \text{ km}$  on dayside; below

650 (above) this altitude, the altitude differences tend in absolute value to be lower (higher) than 13.7  
651 km. Above this altitude range, transport processes are dominant, while below this altitude range,  
652 chemical reactions are dominant. In Figure 1, we have illustrated the effect of increasing  
653 frequency on the visibility of the hyperbola signatures. For example, at 1.52 MHz (panel b) the  
654 signatures are all well pronounced, while at 3.03 MHz (panel e) they become smaller. The  
655 altitude of the level for 1.52 MHz ( $2.86 \times 10^4 \text{ cm}^{-3}$ ) varies from 217 km at  $\text{SZA}=0^\circ$  to 207 km at  
656  $\text{SZA}=85^\circ$ ; this altitude range of 207 - 217 km is found within the transport dominated region.  
657 The altitude of the level for 3.03 MHz ( $1.14 \times 10^5 \text{ cm}^{-3}$ ) reaches 153 km at  $\text{SZA}=0^\circ$ ; this altitude  
658 level is found at altitudes where photochemistry prevails. Bulges are the most commonly  
659 observed structure in the topside ionosphere, present within the transport region with large  
660 altitude differences and present within the photochemical region with small altitude differences.

661         These large and often positive altitude differences PI EDP – edge EDP ( $> 13.7 \text{ km}$ ) at  
662 altitude above  $\sim 200 \text{ km}$  can be related to upward diffusion along vertical crustal magnetic field  
663 lines, in the altitude range of transport regime. This idea was proposed by Matta et al. (2015),  
664 who successfully modeled the formation of density bulges in areas of near radial crustal fields,  
665 using a 2-D ionospheric model incorporating field-aligned transport. Matta et al. (2015) found  
666 that the altitude difference between the density structure and the surrounding normal ionosphere  
667 increases when the altitude increases, starting from  $\sim 170 \text{ km}$  altitude, i.e. at altitudes where  
668 transport becomes important. On the other hand, Matta et al., (2015) did not predict the  
669 formation of bulges at altitudes below  $\sim 170 \text{ km}$ , where they found the ionosphere to have a  
670 photochemical behavior, without any vertical transport effects. In contrast, our observations  
671 show the presence of density structures at altitudes below  $\sim 200 \text{ km}$ , with smaller altitude  
672 differences ( $< 13.7 \text{ km}$ ) becoming increasingly small as altitude decreases. In addition, the entire

673 topside ionosphere seems to move up and down, including the ionospheric peak, in the areas  
674 giving oblique echoes. In these areas, the peak densities did not change predictably. Therefore  
675 we need an additional mechanism which may explain these observations in the altitude range of  
676 photochemical equilibrium. Such mechanism may be as follows.

677           Previous observations of the Martian dayside ionosphere during periods of global dust  
678 storms indicate that the peak altitude and the top of the ionosphere both rise in altitude, while the  
679 peak density does not change much (e.g. Hantsch and Bauer, 1990; Wang and Nielsen, 2003;  
680 Withers et al., 2015). The top of the ionosphere as defined by Withers et al. (2015) is “the  
681 altitude above the peak at which electron densities first fall below  $1500 \text{ cm}^{-3}$  when moving  
682 upward in altitude”. These behaviors are interestingly similar to our observations in areas of  
683 oblique echoes. The mechanism for the dust storm effects has been described by e.g. Wang and  
684 Nielsen (2003) and references therein. During a global dust storm, the lower atmosphere  
685 becomes dusty, and this dust load increases the energy absorption from the Sun, which increases  
686 the neutral temperature of the lower atmosphere. The heated atmosphere then expands and gets  
687 redistributed vertically, such that the neutral density increases in the thermosphere. Maxima in  
688 the neutral density of the upper atmosphere correspond to maxima in the peak altitude. Withers  
689 et al. (2015) found that both the top of the ionosphere and the peak altitude move up and then  
690 down in altitude (by a few tens of km for the top of the ionosphere and a few km for the peak  
691 altitude), as the global dust storms grow and then decay. In analogy, we think there is a possible  
692 heating source (which we discuss later on), localized in areas of near vertical crustal fields which  
693 may locally alter the vertical distribution of the ionizable neutral atmosphere and cause  
694 subsequent raises of the altitude of the density profiles (without affecting the peak densities),  
695 such as we observe in the series of altitude profiles. Both mechanisms mentioned earlier (neutral

696 atmosphere expansion and ionospheric plasma diffusion) may then simultaneously operate in the  
697 regions of near vertical fields, such as to produce density structures in the entire altitude range of  
698 the topside ionosphere.

699         The density structures reoccur in the same areas of magnetic anomalies on the dayside  
700 (Andrews et al., 2014), no matter the field lines being closed or open, even in the absence of  
701 solar wind entries, indicating that that their formation does not require magnetic reconnection  
702 between the IMF and the magnetic anomalies (e.g. Diéval et al., 2015). We note that field-  
703 aligned diffusion indeed occurs whatever the field lines are open or closed. Furthermore a  
704 heating source may further enhance the density structures by either causing an expansion of the  
705 neutral atmosphere (a given electron density level will rise in altitude) or by increasing the  
706 electron temperature leading to reduced recombination rates and thus larger plasma densities  
707 (Andrews et al., 2014). Diéval et al. (2015) based on their observations rejected the hypothesis  
708 that the dayside bulges are primarily driven by ionization/heating input from precipitating solar  
709 wind electrons, which had been proposed by earlier studies (Andrews et al., 2014, and references  
710 therein). However, solar wind precipitation and other processes may still contribute to strengthen  
711 existing density structures, as we will see below.

712         The status of the density structures changes as the planet rotates. The plasma density  
713 decreases due to electron-ion recombination when it enters the shadow. The nightside densities  
714 are often below  $5000 \text{ cm}^{-3}$  (the lowest densities detectable by MARSIS AIS), so in practice  
715 seldom detectable (Němec et al., 2010). However, Němec et al. (2011b) have reported  
716 intermittent observations of elevated electron peak densities in areas of near radial crustal fields  
717 with frequent open-field line topology during nighttime. They were detected via oblique echoes,  
718 indicating that these density structures were inclined plasma layers. Diéval et al. (2014) found



719 that such cases of high peak densities on nightside tend to be observed simultaneously with  
720 precipitating tens to hundreds eV electrons (auroral or magnetotail), above the strong magnetic  
721 anomalies of the Southern hemisphere, at times when the IMF points Westward. Additional  
722 heating and ionization by energetic electron entries was thus necessary for the densities to  
723 become large enough to become detectable by MARSIS (Diéval et al., 2014; Němec et al.,  
724 2011b). Diéval et al. (2015) postulated that a recurrent process independent from external  
725 conditions causes the density structures to reform during daytime in areas of near radial crustal  
726 fields, and thereafter they would disappear during nighttime due to plasma densities becoming  
727 too low to be measured. These authors suggested that these structures would be sporadically  
728 enhanced at times of energetic electron precipitation driven by external conditions, making them  
729 observable by MARSIS. The observations reported here imply that this recurrent process  
730 involves transport (of plasma and/or of neutrals).

731 In general, the dayside electron densities at altitudes  $> 300$  km are greater in areas of  
732 crustal fields than in areas without (e.g. Andrews et al., 2013; 2015). At these high altitudes, the  
733 ionosphere is in the transport regime. This difference may occur due to a facilitated vertical  
734 transport of plasma along near vertical crustal field lines, while such vertical transport is  
735 inhibited in areas where the interplanetary magnetic field (nearly horizontal orientation on  
736 dayside, e.g. Brain et al., 2003) is free to permeate low altitudes. At the same time, the planetary  
737 plasma is trapped within the mini-magnetospheres (e.g. Ramstad et al., 2016), where the solar  
738 wind seldom has access and can thus not trigger ion loss, which keeps plasma densities high.  
739 Similarly, plasma scale heights were found to be larger at 200 - 250 km altitudes, than at 150 -  
740 200 km altitudes, in areas of near-radial crustal fields, due to the facilitated upward diffusion of  
741 plasma along the field lines (e.g. Ness et al., 2000).

742           There have been reports of sporadically elevated peak densities in areas of near radial  
743   crustal fields on the dayside (Duru et al., 2016; Fallows et al., 2016, presented at DPS meeting  
744   #48; Nielsen et al., 2007b). We note that they are not necessarily related to the (recurrent)  
745   formation of density structures, but may happen simultaneously and enhance the structures  
746   further. Nielsen et al. (2007b) found no simultaneous observations of precipitating plasma/X-ray  
747   flux able to explain cases of high densities at low altitude. They invoked the reduction of the  
748   electron-ion recombination rate due to Joule heating of atmospheric neutrals by AC electric  
749   fields related to plasma instabilities in areas of open crustal field lines. Finally, Duru et al. (2016)  
750   have observed, in an area of strong near vertical crustal fields, a dayside case with simultaneous  
751   detection of: local plasma depletion at spacecraft altitude, peak density enhancement, and  
752   oblique echoes. They postulated that an earlier instance of magnetic reconnection between the  
753   crustal fields and the IMF allowed accelerated precipitating electrons to reach low altitudes along  
754   open field lines, providing heating and ionization which may have strengthened a density  
755   structure already present, and at the same time driving energization and outflow of planetary ions  
756   such as to form a density cavity at high altitude. They suggested that the increased peak electron  
757   density may have been caused by either the Nielsen et al. (2007b) mechanism or the electron  
758   precipitation.

759           We note that although the dayside oblique echoes are commonly observed above  
760   magnetic anomalies, plasma depletions and peak density enhancements are on the other hand  
761   rarely observed during daytime (Duru et al., 2016; Fallows et al., 2016, presented at DPS  
762   meeting #48; Hall et al., 2016). On the dayside, enhanced peak densities are found in areas of  
763   near radial fields being more often open than usual and can be detected via oblique echoes  
764   (Fallows et al., 2016, presented at DPS meeting #48), similar to their nightside counterparts

765 (Němec et al., 2011b). From the Duru et al. (2016) case, we infer that whatever the shape  
766 distribution of the target of oblique echoes was when it formed, sporadic processes appear to  
767 have altered its shape distribution into: presumably a dip at MEX location and a bulge near the  
768 ionospheric peak.

769 The methodology of the present work focuses on the study of time series of EDPs at  
770 selected frequencies, to study horizontal density gradients. Another interesting way to study the  
771 topside ionosphere is to examine the vertical structure of the ionosphere, with single EDPs  
772 obtained either by inversion of ionograms or by radio occultation technique, to identify vertical  
773 density gradients (e.g. Kopf et al., 2008; Withers et al., 2005).

774 Withers et al. (2005) observed that density bumps and bite-outs can exist in regions of  
775 strong magnetic anomalies and that their occurrence seemed to depend on the crustal field  
776 inclination and azimuth. The altitudes of these features were found within the dynamo region of  
777 the Martian ionosphere, which exists between 120 and 190 km altitude for a magnetic field  
778 strength of 100 nT, as estimated by Withers et al. (2005). These authors suggested the role of  
779 neutral winds, magnetic field, and ionized plasma, within the dynamo region, to generate  
780 induced ionospheric currents and associated magnetic fields, which could modify the density  
781 profiles such as to create bite-outs or bumps. Field-aligned currents and Pedersen currents in  
782 magnetic cusp areas were simulated by e.g. Fillingim et al. (2010, 2012); Rioussset et al. (2013,  
783 2014). Such currents are expected to always be present, and can be a recurrent source of heating  
784 of the neutral atmosphere, localized to regions of magnetic cusps. Heating at altitudes below the  
785 ionospheric peak, could cause the typically higher altitudes we have observed for the entire  
786 topside ionosphere in these regions.

787           Kopf et al. (2008) have discovered the existence of transient topside layers above the  
788 main ionospheric peak, at typical altitudes 180-240 km on the dayside, with an occurrence rate  
789 decreasing when going from the subsolar region to the terminator (from 60% to 5% of  
790 observation time). The topside layers are found mostly in regions of low crustal magnetic field  
791 strength (e.g. Kim et al., 2012, Kopf et al., 2017). It is not known whether topside layers exist in  
792 regions of stronger crustal fields, because the presence of electron cyclotron harmonics in the  
793 ionograms can hinder the visibility of the ionospheric traces at low frequency, including any  
794 potential topside layer. Concurrent measurements of topside layers by MARSIS onboard the  
795 MEX orbiter and by the in-situ particle and field package onboard the MAVEN orbiter indicate  
796 localized increases in the in-situ electron density and total ion density in the vicinity of the  
797 topside layers detected remotely by MARSIS (Kopf et al., 2017). These authors also found  
798 simultaneous magnetic field rotations and magnetic field dips, attributed to current sheets.

799           We remark that these topside layers have two characteristics which are incompatible with  
800 the characteristics of the density structures investigated in the present work: the former are  
801 transient and are detected away from regions of significant crustal fields (but could possibly exist  
802 in such regions although non detectable due to cyclotron harmonics), while the latter reoccur  
803 regularly and only above regions of significant crustal fields. In addition, the former have been  
804 attributed to various mechanisms involving the solar wind interaction with the topside  
805 ionosphere (e.g. Kopf et al., 2017), while the latter seem to have no relationship to the upstream  
806 solar wind conditions or to the presence/absence of magnetosheath plasma entries at MEX  
807 altitude (e.g. Andrews et al., 2014, Diéval et al., 2015). Therefore there seems to be no link  
808 between the topside layers and the regions giving oblique echoes. Another indication that these  
809 ionospheric features are independent is that topside layers can be present and give oblique echoes

810 if found in areas where the main ionosphere layer already gives oblique echoes, but are not  
811 present otherwise (Venkateswara Rao et al., 2017).

812         Bulges may be the primary type of density structure to appear, as modelled in the simple  
813 case of vertical diffusion by Matta et al. (2015). They are the most observed simplest shape.  
814 Other shapes likely require more complex conditions. The formation of slopes may be related to  
815 gradients in the ability of the plasma to be transported, favoring convex slopes or concave slopes  
816 depending on circumstances. Dips possibly form as a result of ion outflow along open field lines  
817 at occasions of magnetic reconnection between the IMF and the crustal fields, during which the  
818 solar wind is able to energize the planetary ions within the mini-magnetosphere. It is also  
819 possible that a magnetic arcade near the terminator possesses one footprint on dayside and the  
820 other footprint on nightside, such that electrons produced on dayside are lost on nightside after  
821 travelling along the arcade (e.g. Xu et al., 2016): this may cause a dip within the illuminated area  
822 of near-radial field lines. The restriction of our study to  $SZA < 85^\circ$  certainly limits the  
823 observation of this situation. Instead we are working here with the commonly observed dayside  
824 events where both footprints of the corresponding magnetic arcades are reasonably expected to  
825 be illuminated. A decrease of the altitude level at selected frequencies could also be brought by  
826 the contracting and cooling of the underlying atmosphere, after a transient heating source (such  
827 as from solar wind precipitation) has subsided.

828

## 829 5) Summary

830         This paper reports a statistical study of oblique ionospheric echoes in the dayside Martian  
831 ionosphere identified with the MARSIS AIS radar data. The reflecting targets for these oblique

832 echoes are non-horizontal localized electron density structures associated to regions of near  
833 radial crustal magnetic fields. The altitude variations (shape) of 48 density structure events  
834 corrected for signal dispersion have been investigated through time series of EDPs, by  
835 comparing a reference EDP (PI EDP) to the other EDPs in the same time series. We obtained the  
836 following results:

837 1. The altitude differences between the PI EDP and the edge EDPs tend to be larger at low  
838 frequencies (high altitudes) and smaller at high frequencies (low altitudes), with values going  
839 from a few tens of km down to a few km as frequency increases (equivalently altitude  
840 differences of a few tens of % down to a few % relative to the altitude of the PI EDP). The  
841 density structures are found with large altitude variations in the region of transport regime (above  
842 ~200 km altitude), and with smaller altitude variations in the region of photochemistry regime  
843 (below ~200 km altitude).

844 2. The inspection of the hyperbola signatures in echograms at selected frequencies indicates  
845 that oblique echoes are more developed at low frequency than at high frequency, which is  
846 consistent with the altitude differences between PI EDP and edges EDPs to be larger (more tilted  
847 density contour) at low frequency than at high frequency, and agrees with the result from Nielsen  
848 et al. (2007a).

849 3. There are four simplest possible shapes for inclined structures able to give oblique  
850 echoes: bulge, dip, uphill slope and downhill slope. Uphill slopes and downhill slopes can be  
851 concave or convex. Convex slope events resemble dips (downward swell) and concave slope  
852 events resemble bulges (upward swells).

853 4. A given event may keep the same shape over all frequencies or change shape over  
854 frequency. The changes of shape over frequency are gradual, but systematic, with natural  
855 transitions between bulge and dip, separated by concave and convex slope events in the right  
856 order.

857 5 The comparison of the time series of EDPs at selected frequencies with the 1.8 - 2 MHz  
858 integrated echograms for individual events brings intriguing results. The apparent altitude of the  
859 apex of the hyperbola signature in the echograms does not vary consistently with the altitude  
860 levels corrected for dispersion: the apex of the hyperbola does not necessarily correspond to the  
861 highest (or lowest) real altitude level in the time series. The presence of one or two clear legs or  
862 short/unclear legs in the hyperbola signature does not seem to relate to the simplest shape in the  
863 EDP time series (it may be any of these: bulge, dip, downhill and uphill slopes).

864 6. In most of the frequency range of the EDPs, the number of bulges dominates the numbers  
865 of other shapes. The number of bulges peaks at a fixed frequency 2.111 MHz, much higher than  
866 for the other shapes: the numbers of uphill slopes, downhill slopes and dips peak at a fixed  
867 frequency of 1.63, 1.455, and 1.52 MHz, respectively.

868 7. At a given frequency, the altitude differences between the PI EDP and the edge EDPs tend  
869 to be larger in absolute value for bulges than for other shapes. It is possible that the smaller  
870 altitude differences of uphill slope, downhill slope and dip events could be a bias from their  
871 small numbers. The median altitude difference we have determined for bulges at a fixed  
872 frequency 1.848 MHz is 12.4 km, which is of the same order as the rms apparent altitude of 19  
873 km at a fixed frequency 1.8 MHz reported by Duru et al. (2006).

874 8. The examination of the entire frequency range of the EDPs in the time series of individual  
875 events indicates the possible presence of topside layers, density bumps and density bite-outs (e.g.  
876 Kopf et al., 2008, Withers et al., 2005) in the form of slight ledges in the vertical structure. Also,  
877 the altitude level at a fixed frequency 1.936 MHz clearly increases when the ionospheric peak  
878 altitude increases, and has a weak increasing trend when the peak density increases. The entire  
879 topside ionosphere seems to move up and down in areas giving oblique echoes.

880 9. The latitude extension of the areas giving oblique echoes, which is usually comparable to  
881 the latitude extension of the corresponding magnetic cusps, permits a sampling of a wide range  
882 of crustal field orientations, from near-vertical up to near-horizontal. There is a tendency for  
883 more vertical crustal fields toward the center of the density structures, and more horizontal fields  
884 toward the edges.

885 10. At a fixed frequency 1.936 MHz, the relative altitude differences between the PI EDP and  
886 the other EDPs in the time series of individual events, and the classification into the 4 possible  
887 simplest shapes, seem to be independent or weakly dependent upon the crustal field orientation,  
888 and vary for events located in geographical proximity (within 10° longitude) but detected at  
889 different dates and times.

890 Transport appears to be a key element in the formation of density structures. Two  
891 recurrent mechanisms based on transport could operate, possibly at the same time: 1) field-  
892 aligned diffusion of plasma along near radial (open or closed) field lines, 2) electron density  
893 levels rising in altitude through the expansion of the ionizable neutral atmosphere presumably  
894 due to localized Joule heating by ionospheric currents at magnetic cusps. Other mechanisms may  
895 alter the density structures either by enhancing them or weakening them. Heating/ionization by



896 electron precipitation or AC electric fields may further increase the plasma densities in areas of  
897 near-radial open crustal fields.

898 In-situ measurements in the altitude range of the density structures would be a valuable  
899 complement to the remote measurements enabled by MARSIS AIS. In particular, future studies  
900 making use of the rich combined capabilities of Mars Express and MAVEN would help  
901 understand the formation and evolution of individual structures, in particular, more in-situ  
902 measurements of downhill slopes, uphill slopes and dips are needed. Future studies also need to  
903 evaluate ray tracing of radio signals through models of ionospheric layers to study the  
904 characteristics of oblique echoes; they would also be very useful to understand the intriguing  
905 results brought by the comparison of EDP time series and echograms.

906

## 907 Appendix A

908 The derived altitude profiles of Morgan et al. (2013) make two assumptions: vertical  
909 propagation and plane parallel stratification. Here we discuss potential issues in applying these  
910 assumptions in regions of density structures. Morgan et al. (2013) warned about the use of the  
911 profiles in the areas of oblique echoes, because the assumption of vertical propagation may not  
912 be true. In fact the single ionospheric echo received may be vertical or oblique depending on the  
913 density layer inclination at the reflection point. We note that MARSIS measures only the time  
914 delay to receive the echo, without knowledge of the angle between the echo direction and the  
915 nadir. This time delay is given as input to the inversion routine, which outputs the range  
916 corrected for dispersion. The inversion itself does not need the direction of the echo. It is only  
917 afterwards, at the stage of calculating the altitude of the obtained profile that the assumption of

918 vertical propagation is made: layer altitude = MEX altitude – layer range. Given that the  
919 reflection angle cannot be known, it is not possible to account for this angle to amend the layer  
920 altitude. Thus in practice we can only use the altitudes as derived with the nadir echo  
921 assumption. On the other hand, the assumption of plane parallel stratification is applied inside  
922 the inversion routine and is thus required at an early stage to produce a range corrected for  
923 dispersion. Given the trend of the altitude differences PI EDP – edge EDP to increase over  
924 frequency (Figure 7), one may then wonder whether the density structures still respect a plane  
925 parallel stratification over their whole frequency range. Below we check the validity of these two  
926 assumptions, for the events in our list, by using information from the Results Section.

927 We want to determine the angle that the inclined layer makes with the horizontal for  
928 different frequencies by considering a line joining the PI altitude and the edge altitude (beginning  
929 or end), and the angle between such successive inclined layers of consecutive frequencies. We  
930 care about how large the angles are, so we take their absolute values. In practice, it means  
931 changing all the events into bulges (absolute value of altitude differences for both edges), which  
932 is good for our purpose, especially since the majority of the events are bulges. Then we simplify  
933 the shape of the structures by keeping only the altitude variations of the edge EDPs and the PI  
934 EDP, ignoring the profiles in between, which effectively turns the shapes into triangles. Finally  
935 we can calculate, for each frequency  $f$ , the angle  $\alpha_f$  between a horizontal line at the altitude of  
936 the edge point and a line joining the altitudes of the edge and PI points:  $\tan \alpha_f = H_f/D$ . Here  
937  $H_f$  is the absolute value of the altitude difference PI EDP – edge EDP at frequency  $f$  and  $D$  is the  
938 horizontal distance traveled by MEX between the edge and PI times (using the MEX velocity  
939 and the absolute value of the time difference between edge and PI). This is done separately for  
940 the beginning and end edges. Then we deduce the angle  $\theta_{f_2 f_1}$  between two successive inclined

941 density layers of consecutive frequencies  $f_1$  and  $f_2$  ( $f_2 > f_1$ ) as  $\theta_{f_2 f_1} = \alpha_{f_2} - \alpha_{f_1}$  .  
942 Remark: the density layer is very likely to be horizontal or near horizontal both at the edge point  
943 (because it is very close to the surrounding normal ionosphere) and at the PI point (especially for  
944 a bulge or a dip), so we can use these altitude values directly, with the nadir echo assumption.

945 Figure A1 shows the distributions of the angle  $\alpha_f$  (panel a) and the angle  $\theta_{f_2 f_1}$  (panel b),  
946 as a function of frequency, for all the events, for both the beginning and end edges, plotted as  
947 grey dots. The red dots correspond to the median angles versus frequency. Since  $\alpha_f$  is  
948 proportional to  $H_f$ , the angle between horizontal and inclined layer tends to increase when the  
949 frequency decreases (panel a), just like the altitude difference does increase. The distribution of  
950 angles broadens as frequency decreases, the angle increases from a few degrees at high  
951 frequency, up to  $\sim 15^\circ$  at low frequency, confirmed by the increasing trend of the median values  
952 from  $3.4$  to  $4.5^\circ$ . Therefore, for these events, the inclined layers from the edge point to the PI  
953 point are weakly inclined to the horizontal, with angles typically small at all frequencies. Then,  
954 the distribution of  $\theta_{f_2 f_1}$  does not vary over frequency (panel b), remaining close to zero at all  
955 frequencies: the angles between successive layers vary mostly up to  $0.5^\circ$ , with the median values  
956 remaining  $\leq 0.1^\circ$ . Therefore these density layers are making negligible angles to each other at all  
957 frequencies, and basically appear as parallel strata from the edge point to the PI point. We  
958 conclude that for our list of density structures, the assumption of plane parallel stratification is  
959 certainly valid, and the assumption of vertical reflection is, although not exactly true, good  
960 enough as approximation. Therefore we are confident that these EDPs are valid and provide  
961 useful insight for these particular density structures.

962 For comparison, Nielsen et al. (2007a) estimated the angles of inclined layers to the  
963 vertical for a few cases of density structures, with a different hypothesis (assuming a fixed  
964 altitude for the reflection point), and found a wide range of values from 5 to 90°. We note that  
965 the assumption of vertical propagation is certainly not applicable for strongly inclined structures,  
966 and thus the vertical profiles would be invalid in this case.

967

968 Acknowledgements: CD and JAW were supported by grant ST/M001059/1 from the UK Science  
969 and Technology Facilities Council. AJK was supported by NASA through contract 1560641 with  
970 the Jet Propulsion Laboratory. The MARSIS data are available on  
971 <ftp://psa.esac.esa.int/pub/mirror/MARS-EXPRESS/MARSIS/>. CD thanks F. Němec (email  
972 address: frantisek.nemec@gmail.com) for providing updated MARSIS AIS EDPs.

973

974 References:

975 Acuña, M. H., et al. (1999), Global distribution of crustal magnetization discovered by the Mars  
976 Global Surveyor MAG/ER experiment, *Science*, 284(5415), 790–793,  
977 doi:10.1126/science.284.5415.790

978 Andrews, D. J., et al. (2013), Determination of local plasma densities with the MARSIS radar:  
979 Asymmetries in the high-altitude Martian ionosphere, *J. Geophys. Res.*, 118, 6228–6242,  
980 doi:10.1002/jgra.50593

981 Andrews, D. J., et al. (2014), Oblique reflections in the Mars Express MARSIS data set: Stable  
982 density structures in the Martian ionosphere, *J. Geophys. Res.*, 119, 3944–3960,  
983 doi:10.1002/2013JA019697

984 Andrews, D. J., et al. (2015), Control of the topside Martian ionosphere by crustal magnetic  
985 fields, *J. Geophys. Res.*, 120, 3042–3058, doi:10.1002/2014JA020703

986 Barabash, S., et al. (2006), The Analyzer of Space Plasmas and Energetic Atoms (ASPERA-3)  
987 for the Mars Express Mission, *Space Sci. Rev.*, 126(1–4), 113–164, doi:10.1007/s11214-006-  
988 9124-8

989 Brain, D. A., et al. (2003), Martian magnetic morphology: Contributions from the solar wind and  
990 crust, *J. Geophys. Res.*, 108(A12), 1424, doi:10.1029/2002JA009482

991 Brain, D. A., et al. (2007), Electron pitch angle distributions as indicators of magnetic field  
992 topology near Mars, *J. Geophys. Res.*, 112, A09201, doi:10.1029/2007JA012435

993 Budden, K. G. (1961), *Radio Waves in the Ionosphere*, Cambridge Univ. Press, Cambridge, U. K

994 Cain, J. C., et al. (2003), An  $n = 90$  internal potential function of the Martian crustal magnetic  
995 field, *J. Geophys. Res.*, 108(E2), 5008, doi:10.1029/2000JE001487

996 Diéval, C., et al. (2014), MARSIS observations of the Martian nightside ionosphere dependence  
997 on solar wind conditions, *J. Geophys. Res.*, 119, 4077–4093, doi:10.1002/2014JA019788

998 Diéval, C., et al. (2015), MARSIS remote sounding of localized density structures in the dayside  
999 Martian ionosphere: A study of controlling parameters, *J. Geophys. Res.*, 120, 8125–8145,  
1000 doi:10.1002/2015JA021486

1001 Duru, F., et al. (2006), Magnetically controlled structures in the ionosphere of Mars, *J. Geophys.*  
1002 *Res.*, 111, A12204, doi:10.1029/2006JA011975

1003 Duru, F., et al. (2010), Overlapping ionospheric and surface echoes observed by the Mars  
1004 Express radar sounder near the Martian terminator, *Geophys. Res. Lett.*, 37, L23102,  
1005 doi:10.1029/2010GL045859

1006 Duru, F., et al. (2016), A case study of a density structure over a vertical magnetic field region  
1007 in the Martian ionosphere, *Geophys. Res. Lett.*, 43, 4665–4672, doi:10.1002/2016GL068686

1008 Fallows, K., et al. (2016), Oblique echoes at unusually high frequencies in MARSIS-AIS  
1009 measurements of the topside ionosphere of Mars, American Astronomical Society, DPS meeting  
1010 #48, id.220.33

1011 Fillingim, M. O., et al. (2010), Localized ionization patches in the nighttime ionosphere of Mars  
1012 and their electrodynamic consequences, *Icarus*, 206(1), 112–119,  
1013 doi:10.1016/j.icarus.2009.03.005

1014 Fillingim, M. O., et al. (2012), On wind-driven electrojets at magnetic cusps in the nightside  
1015 ionosphere of Mars, *Earth Planets Space*, 64(2), 93–103, doi:10.5047/eps.2011.04.010

1016 Fox, J. L., and K. E. Yeager (2006), Morphology of the near-terminator Martian ionosphere: A  
1017 comparison of models and data, *J. Geophys. Res.*, 111, A10309, doi:10.1029/2006JA011697

1018 Gurnett, D. A., et al. (2005), Radar soundings of the ionosphere of Mars, *Science*, 310(5756),  
1019 1929–1933, doi:10.1126/science.1121868

1020 Hall, B. E. S., et al. (2016), A survey of superthermal electron flux depressions, or “electron  
1021 holes,” within the illuminated Martian induced magnetosphere, *J. Geophys. Res.*, vol. 121(5),  
1022 4835–4857, doi: 10.1002/2015JA021866

1023 Hantsch, M. H., and Bauer S. J. (1990), Solar control of the Mars ionosphere, *Planetary and*  
1024 *Space Science*, vol. 38, 539-542, doi: 10.1016/0032-0633(90)90146-H.

1025 Kim, E., et al. (2012), The Analysis of the Topside Additional Layer of Martian Ionosphere  
1026 Using MARSIS/Mars Express Data, *J. Astron. Space Sci.*, 29(4), 337-342, doi:  
1027 10.5140/JASS.2012.29.4.337

1028 Kopf, A. J., et al. (2008), Transient layers in the topside ionosphere of Mars, *Geophys. Res. Lett.*,  
1029 35, L17102, doi:10.1029/2008GL034948

1030 Kopf, A. J., et al. (2017), The transient topside layer and associated current sheet in the  
1031 ionosphere of Mars, *J. Geophys. Res.*, 122, 5579–5590, doi:10.1002/2016JA023591

1032 Matta, M., et al. (2015), Interpreting Mars ionospheric anomalies over crustal magnetic field  
1033 regions using a 2-D ionospheric model, *J. Geophys. Res.*, 120, 766–777,  
1034 doi:10.1002/2014JA020721

1035 Morgan, D. D., et al. (2008), Variation of the Martian ionospheric electron density from Mars  
1036 Express radar soundings, *J. Geophys. Res.*, 113, A09303, doi:10.1029/2008JA013313

1037 Morgan, D. D., et al. (2013), The processing of electron density profiles from the Mars Express  
1038 MARSIS topside sounder, *Radio Sci.*, 48, 197–207, doi:10.1002/rds.20023

1039 Nagy, A., et al. (2004), The plasma Environment of Mars, *Space Sci. Rev.*, 111(33),  
1040 doi:10.1023/B:SPAC.0000032718.47512.92

1041 Němec, F., et al. (2010), Nightside ionosphere of Mars: Radar soundings by the Mars Express  
1042 spacecraft, *J. Geophys. Res.*, 115, E12009, doi:10.1029/2010JE003663

1043 Němec, F., et al. (2011a), Dayside ionosphere of Mars: Empirical model based on data from the  
1044 MARSIS instrument, *J. Geophys. Res.*, 116, E07003, doi:10.1029/2010JE003789

1045 Němec, F., et al. (2011b), Areas of enhanced ionization in the deep nightside ionosphere of  
1046 Mars, *J. Geophys. Res.*, vol. 116, E06006, doi:10.1029/2011JE003804

1047 Němec, F., et al. (2016a), On improving the accuracy of electron density profiles obtained at  
1048 high altitudes by the ionospheric sounder on the Mars Express spacecraft, *J. Geophys. Res.*, 121,  
1049 10,117–10,129, doi:10.1002/2016JA023054

1050 Němec, F., et al. (2016b), Empirical Model of the Martian Dayside Ionosphere: Effects of  
1051 Crustal Magnetic Fields and Solar Ionizing Flux at Higher Altitudes, *J. Geophys. Res.*, 121,  
1052 1760-1771, doi: 10.1002/2015JA022060

1053 Ness, N. F., et al. (2000), Effects of magnetic anomalies discovered at Mars on the structure of  
1054 the Martian ionosphere and solar wind interaction as follows from radio occultation experiments,  
1055 *J. Geophys. Res.*, vol. 105(A7), 15991-16004, doi: 10.1029/1999JA000212

1056 Nielsen, E., et al. (2007a), Vertical sheets of dense plasma in the topside Martian ionosphere, *J.*  
1057 *Geophys. Res.*, 112, E02003, doi:10.1029/2006JE002723

1058 Nielsen, E., et al. (2007b), Local plasma processes and enhanced electron densities in the lower  
1059 ionosphere in magnetic cusp regions on Mars, vol. 55(14), 2164–2172, doi:  
1060 10.1016/j.pss.2007.07.003



1061 Picardi, G., et al. (2004), MARSIS: Mars Advanced Radar for Subsurface and Ionospheric  
1062 Sounding, in Mars Express: A European Mission to the Red Planet, edited by A. Wilson, pp. 51–  
1063 69, ESA Publ. Div., Noordwijk, Netherlands

1064 Ramstad, R., et al. (2016), Effects of the crustal magnetic fields on the Martian atmospheric ion  
1065 escape rate, *Geophys. Res. Lett.*, 43, 10,574–10,579, doi:10.1002/2016GL070135

1066 Riousset, J. A., et al. (2013), Three-dimensional multifluid modeling of atmospheric  
1067 electrodynamics in Mars’ dynamo region, *J. Geophys. Res.*, 118, 3647–3659,  
1068 doi:10.1002/jgra.50328

1069 Riousset, J. A., et al. (2014), Electrodynamics of the Martian dynamo region near magnetic cusps  
1070 and loops, *Geophys. Res. Lett.*, 41, 1119–1125, doi:10.1002/2013GL059130

1071 Sánchez-Cano, B., et al. (2016), Solar cycle variations in the ionosphere of Mars as seen by  
1072 multiple Mars Express data sets, *J. Geophys. Res.*, 121, 2547–2568, doi:10.1002/2015JA022281

1073 Venkateswara Rao, N., et al. (2017), Magnetically controlled density structures in the topside  
1074 layer of the Martian ionosphere, *J. Geophys. Res.*, 122(5), 5619–5629, doi:  
1075 10.1002/2016JA023545

1076 Wang, J.-S., and E. Nielsen (2003), Behavior of the Martian dayside electron density peak during  
1077 global dust storms, *Planetary and Space Science*, 51, 329 – 338, doi: 10.1016/S0032-  
1078 0633(03)00015-1

1079 Wang, X.-D., et al. (2009), “Hook” structure in MARSIS ionogram and its interpretation,  
1080 *Geophys. Res. Lett.*, 36, L13103, doi: 10.1029/2009GL038844

1081 Withers, P., et al. (2005), Ionospheric characteristics above Martian crustal magnetic anomalies,  
1082 *Geophys. Res. Lett.*, 32, L16204, doi:10.1029/2005GL023483

1083 Withers, P., et al. (2015), Recovery and validation of Mars ionospheric electron density profiles  
1084 from Mariner 9, *Earth, Planets and Space*, 67-194, doi: 10.1186/s40623-015-0364-2

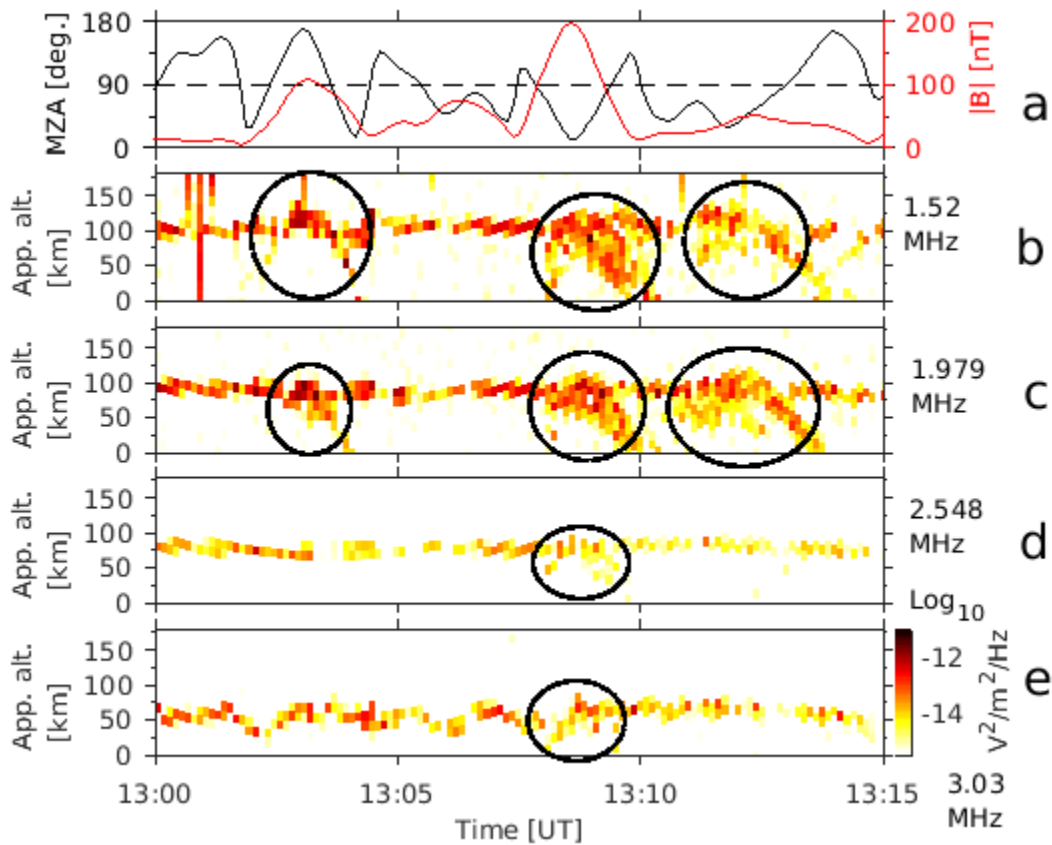
1085 Xu, S., et al. (2016), Deep nightside photoelectron observations by MAVEN SWEA:  
1086 Implications for Martian northern hemispheric magnetic topology and nightside ionosphere  
1087 source, *Geophys. Res. Lett.*, 43, 8876–8884, doi:10.1002/2016GL070527

1088

1089 Figures:

1090

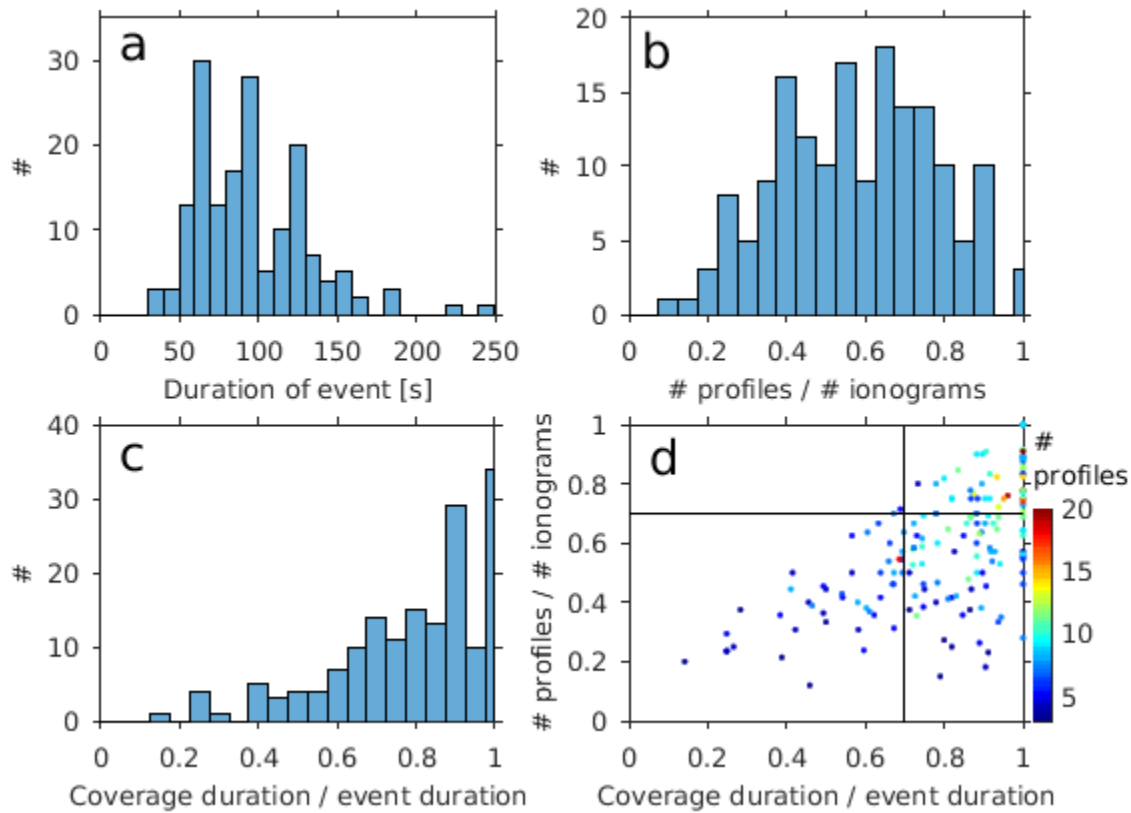
1091



1092

1093 Figure 1: Time series on 22 July 2006, 13:00-13:15 UT, orbit 3253. (a) Crustal magnetic field  
 1094 calculated at 150 km altitude at MEX footprint using the Cain et al. (2003) model: magnetic  
 1095 zenith angle (black curve, left axis) and magnetic field strength (red curve, right axis). The  
 1096 horizontal black dashed line marks the  $90^\circ$  angle (horizontal orientation). (b) to (e) MARSIS  
 1097 echograms at four sounding frequencies: 1.52 (b), 1.979 (c), 2.548 (d) and 3.03 MHz (e); the  
 1098 vertical axis shows the apparent altitude and the color coding shows the received signal spectral  
 1099 density. Black ellipses mark the hyperbola signatures associated to oblique echoes.

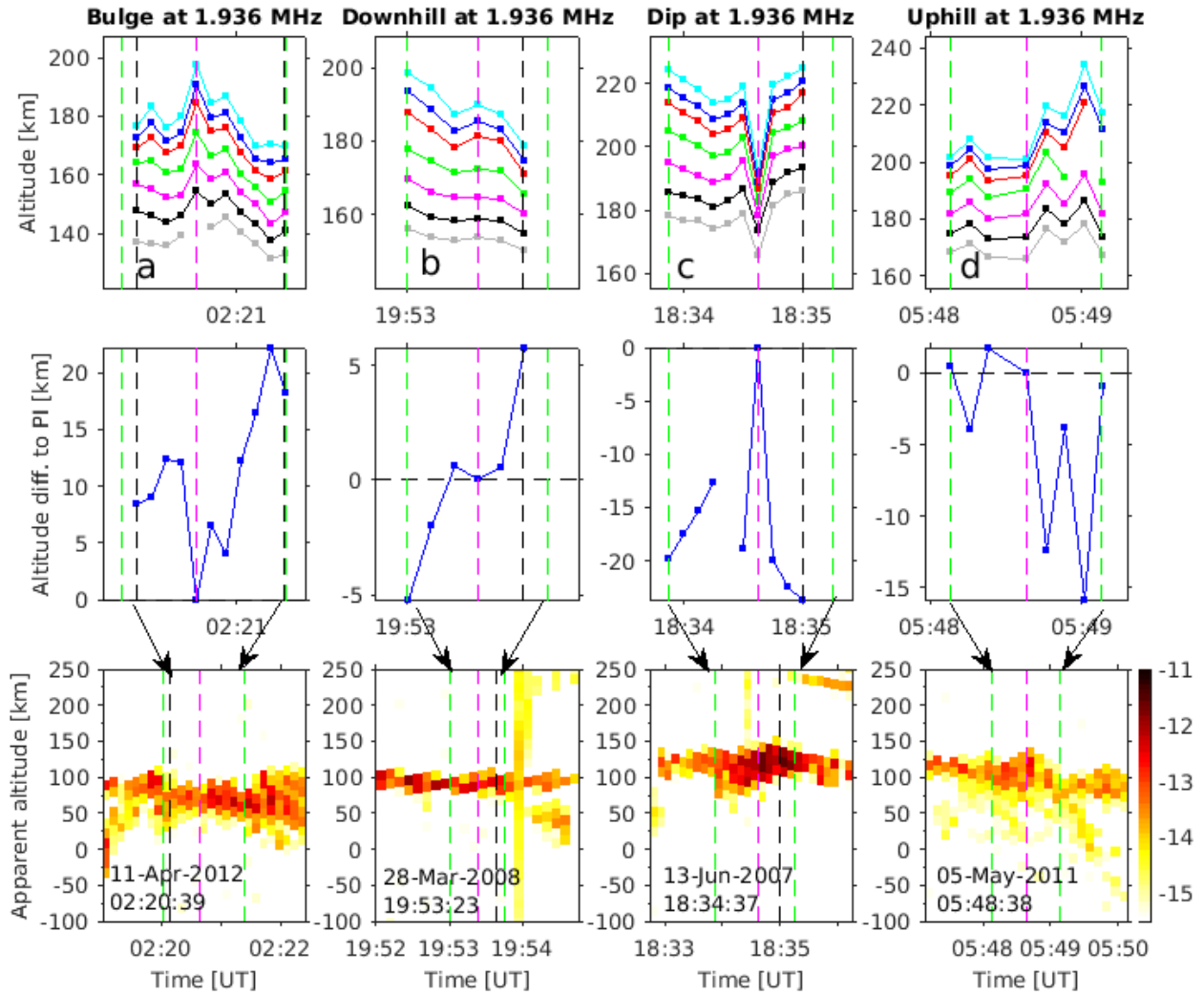
1100



1101

1102 Figure 2: (a) Distribution of event duration for all the events. (b) Distribution of the number of  
 1103 available EDPs divided by the number of ionograms during the duration of each event (ratio of  
 1104 numbers), for all the events. (c) Distribution of the duration of EDP coverage divided by the  
 1105 event duration of each event (ratio of durations), for all the events. (d) Scatter plot of the ratio of  
 1106 durations versus the ratio of numbers, colored by the number of available EDPs during the  
 1107 duration of each event, for all the events. Black solid vertical and horizontal lines are plotted for  
 1108 abscissa=0.7 and ordinate=0.7, respectively. We keep the 48 events for which: number of  
 1109 available EDPs divided by the number of ionograms  $\geq 0.7$  and duration of the EDP coverage  
 1110 divided by the event duration  $\geq 0.7$ .

1111

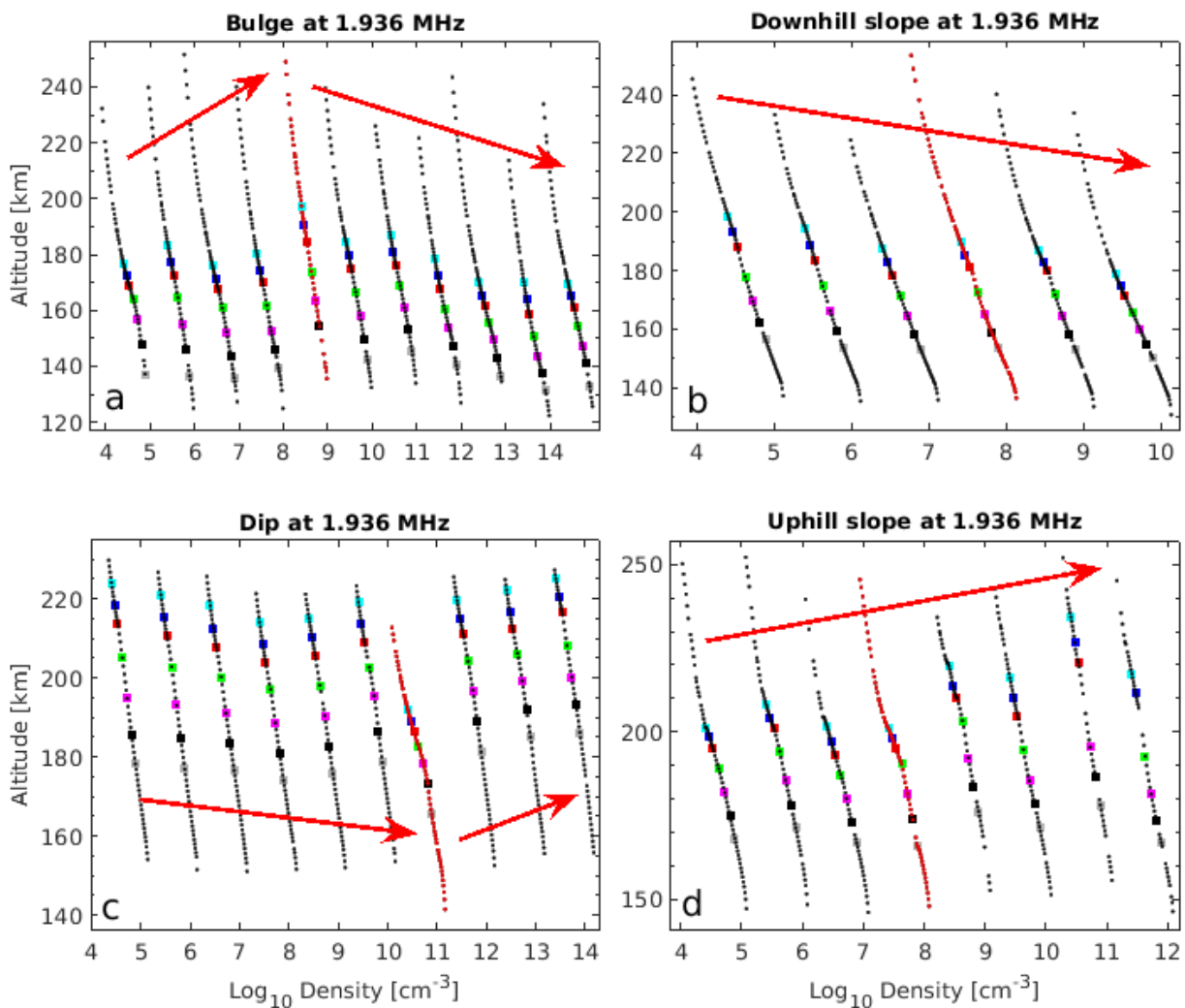


1112

1113 Figure 3: Examples of time series for four events. First column (a): bulge. Second column (b):  
 1114 downhill slope. Third column (c): dip. Fourth column (d): uphill slope. In all panels, the green  
 1115 vertical dashed lines mark the times selected for the beginning and end edges of the hyperbola  
 1116 signature; the black vertical dashed lines mark the times of the first and last available EDPs for  
 1117 the structure; the magenta vertical dashed line marks the time of PI EDP. First row: time series of  
 1118 available EDPs at different frequencies coded by color: 1.433 (cyan), 1.542 (blue), 1.651 (red),  
 1119 1.848 (green), 2.067 (magenta), 2.286 (black) and 2.505 (grey) MHz, corresponding to  $2.55 \times$   
 1120  $10^4$ ,  $2.95 \times 10^4$ ,  $3.38 \times 10^4$ ,  $4.23 \times 10^4$ ,  $5.3 \times 10^4$ ,  $6.48 \times 10^4$  and  $7.78 \times 10^4$   $\text{cm}^{-3}$ . The filled

1121 squares mark the measurement values of altitudes. Second row: time series of altitude difference  
 1122 between the PI EDP and each EDP, for the frequency level 1.936 MHz; values are zero for the PI  
 1123 EDP and for EDPs of identical altitude, positive for EDPs standing lower than the PI EDP,  
 1124 negative for EDPs standing higher than the PI EDP. The horizontal black dashed line marks  
 1125 altitude difference = 0. Third row: echograms integrated between 1.8-2 MHz, in the same format  
 1126 as in Figure 1. Notice the longer time scale shown, indicated by arrows. The date and time for  
 1127 the PI EDP of each event are indicated in the bottom row.

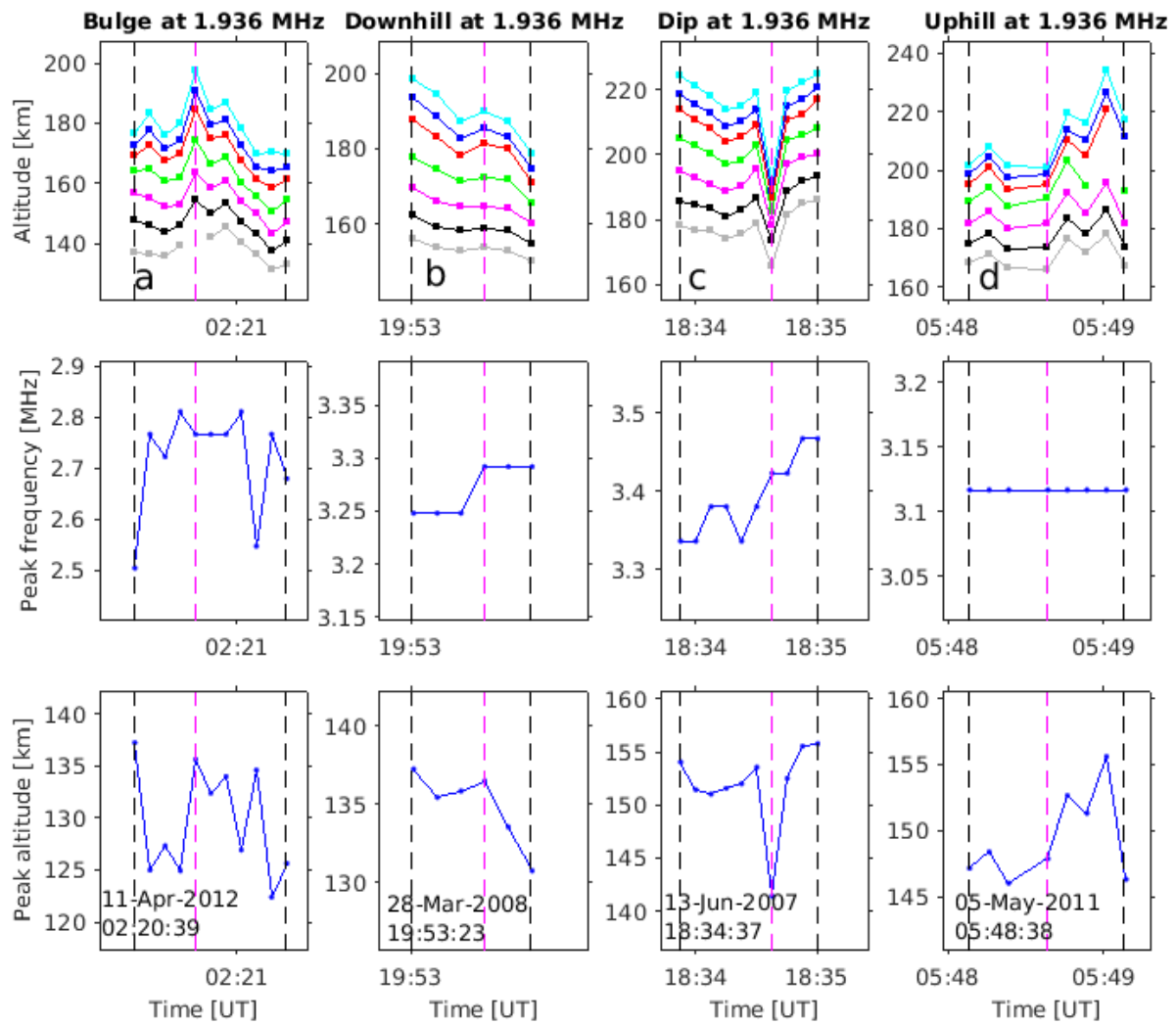
1128



1129

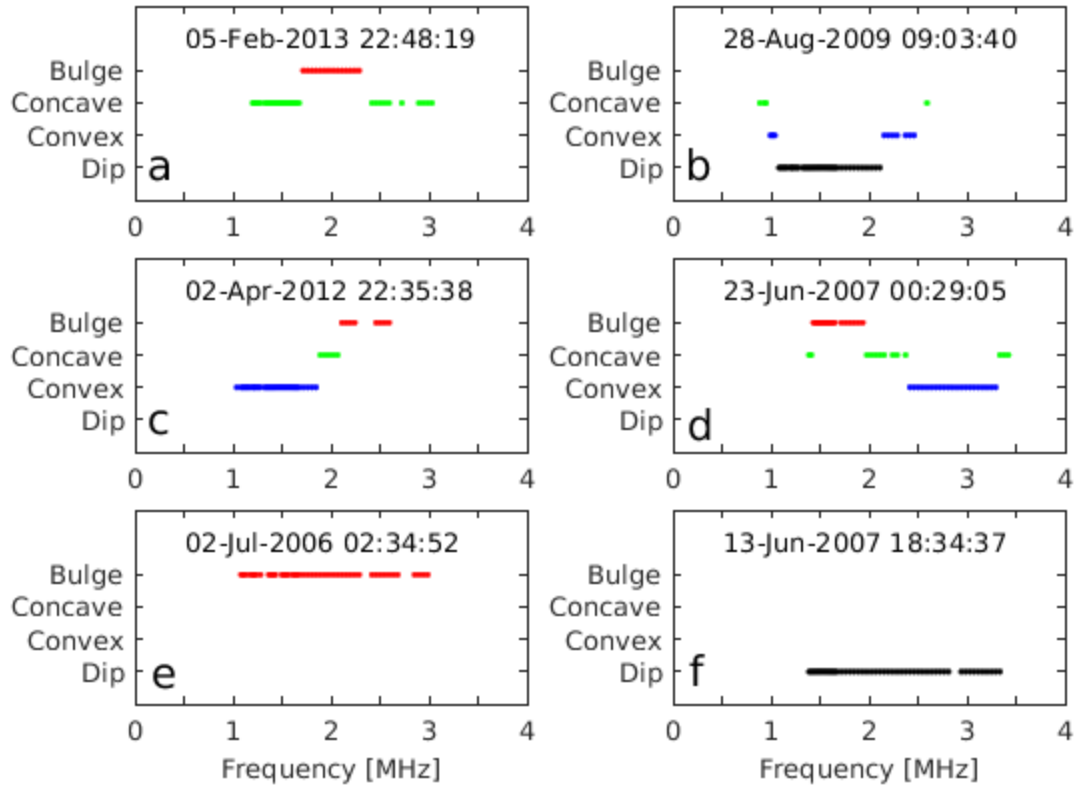
1130 Figure 4: Series of EDPs for the same 4 events: (a) bulge, (b) downhill slope, (c) dip, (d) uphill  
 1131 slope. In each panel, the red curve is the PI EDP; the black curves are the other EDPs for the  
 1132 time series. The local frequency was excluded from analysis; the colored squares represent the  
 1133 same data points as in Figure 3 (same color coding for frequency). For each event, the EDPs are  
 1134 shown versus  $\log_{10}(\text{density})$  in  $\text{cm}^{-3}$ , and the densities of the successive EDPs are multiplied by  
 1135  $10^0, 10^1, 10^2$ , etc., for clarity. Red arrows are added to guide the eye.

1136



1137

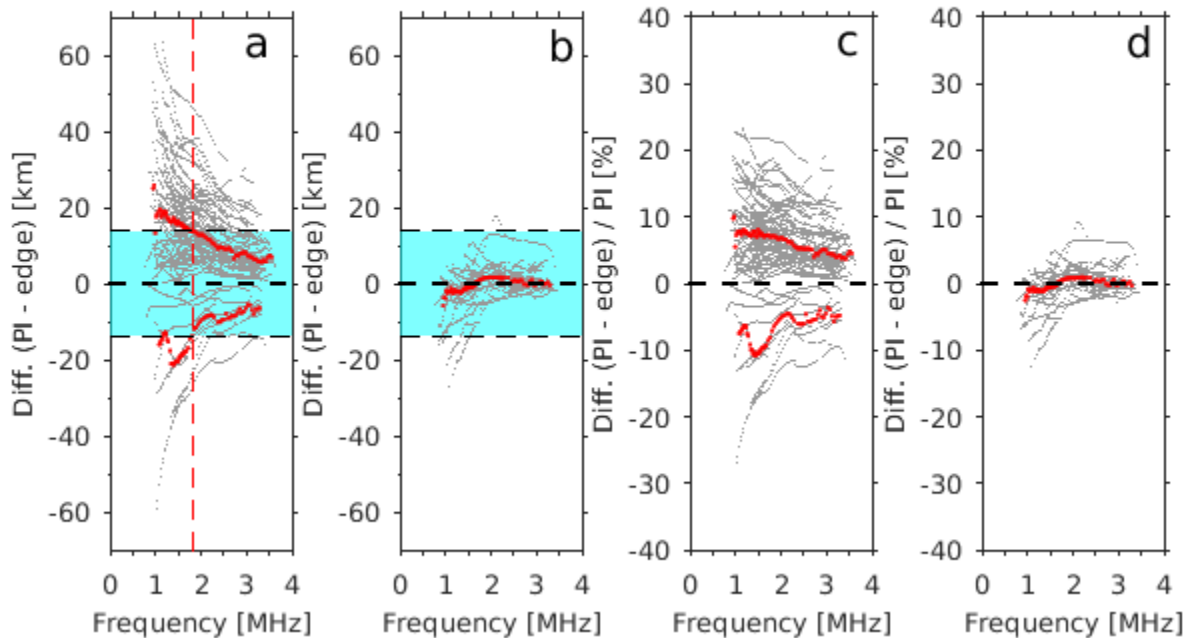
1138 Figure 5: Examples of time series for the same 4 events. First column (a): bulge. Second column  
 1139 (b): downhill slope. Third column (c): dip. Fourth column (d): uphill slope. First row: almost  
 1140 same format as first row of Figure 3. Second row: time series of peak frequency. Third row: time  
 1141 series of peak altitude.



1142  
 1143 Figure 6: Examples of classification of the simplest shape of events as a function of frequency,  
 1144 for 6 events (date and time of PI EDP are indicated in each panel). The vertical axis displays the  
 1145 shape with corresponding colored dots: bulge (red), concave slope (green), convex slope (blue),  
 1146 dip (black). The local frequency was excluded from analysis.

1147  
 1148



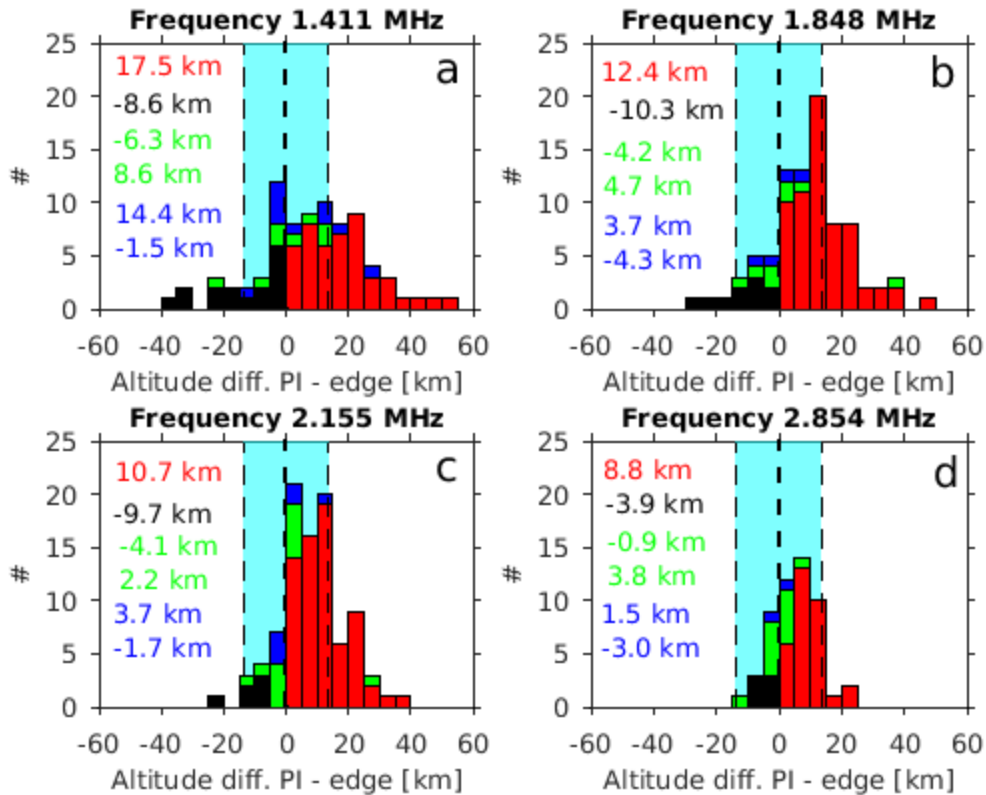


1150

1151 Figure 7: (a,b) Altitude differences PI EDP – edge EDP (in km) for all the events as a function of  
 1152 frequency, plotted as grey lines. (c,d) Altitude differences PI EDP – edge EDP relative to the  
 1153 altitude of the PI EDP (%) for all the events as a function of frequency, plotted as grey lines. The  
 1154 edge EDP refers to either the first EDP or the last EDP of the time series of each event. Altitude  
 1155 differences which change sign over frequency are plotted in columns (b, d), while altitude  
 1156 differences which keep either all-positive or all-negative over frequency are plotted in columns  
 1157 (a, c). The local frequency was excluded from analysis. The red dots indicate the median of the  
 1158 altitude differences as a function of frequency. In panels (a) and (c), the medians are shown  
 1159 separately for the all-positive and the all-negative altitude differences. In panels (a,b), the thin  
 1160 horizontal black dashed lines mark the 13.7 km and -13.7 km thresholds, and the regions with  
 1161  $\text{abs}(\text{altitude difference}) < 13.7 \text{ km}$  are colored in cyan and the regions with  $\text{abs}(\text{altitude}$

1162 difference) > 13.7 km are left in white, to help with clarity. In panel (a), the vertical red dashed  
 1163 line marks the threshold frequency 1.826 MHz (see text).

1164

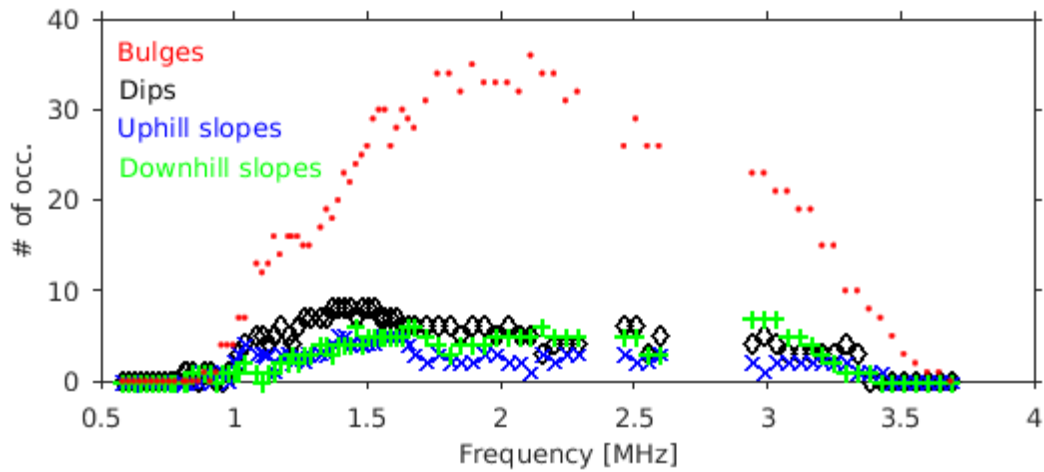


1165

1166 Figure 8: Distributions of altitude differences PI EDP – edge EDP of each event, for all the  
 1167 events, at 4 fixed frequencies: (a) 1.411, (b) 1.848, (c) 2.155 and (d) 2.854 MHz. The edge EDP  
 1168 is either the first or last EDP of the time series of an event. In each panel, the total distribution is  
 1169 separated into stacked color coded distributions for the 4 simplest shapes (same color code as  
 1170 Figure 6): bulge (red), dip (black), uphill slope (blue) and downhill slope (green). This means  
 1171 that in each bin, we count the number of events for each of the four event shapes and then trace  
 1172 colored bars stacked on top of each other; each bar corresponds to one event shape and its length

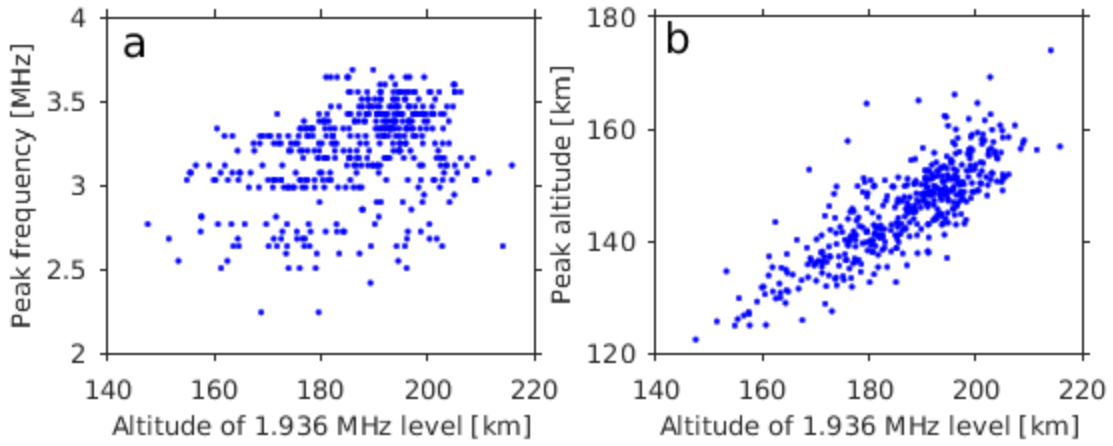
1173 is equal to the number of events. Thin vertical dashed black lines delimitate the regions of  
1174  $\text{abs}(\text{altitude differences}) < \text{or} > 13.7 \text{ km}$ , with corresponding colored patches (cyan or white) for  
1175 clarity. The median values of altitude differences for the different distributions are indicated in  
1176 the panels with the same color code per type of shape.

1177



1178

1179 Figure 9: Distribution of the 4 simplest shapes as a function of frequency, for all the events,  
1180 displayed as colored symbols, with the same color code as Figures 6 and 8: bulges (red dots),  
1181 dips (black diamonds), uphill slopes (blue 'x'), downhill slopes (green '+'). Data points at  
1182 frequency levels within in the sensitivity gaps are not displayed to avoid a bias.

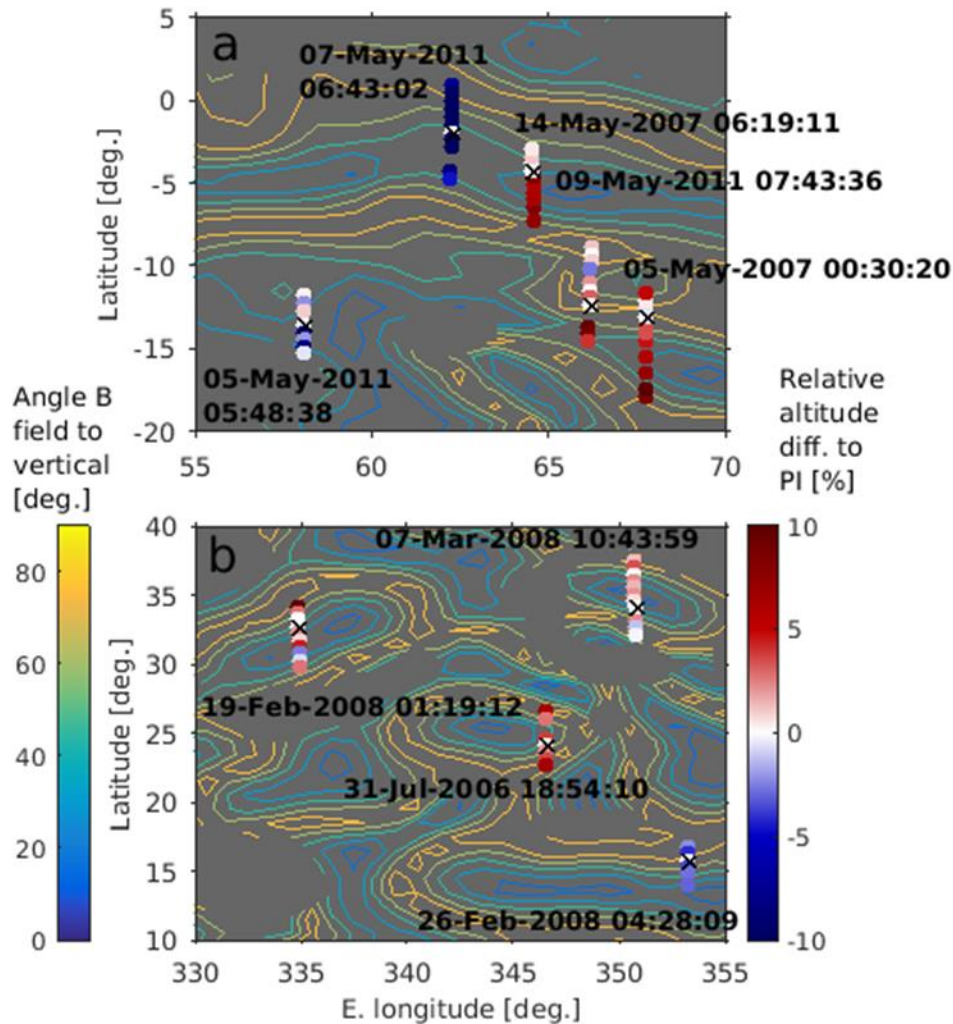


1183

1184 Figure 10: Scatter plot of the altitude level at a fixed frequency 1.936 MHz versus the

1185 ionospheric peak frequency (panel a) and versus the ionospheric peak altitude (panel b).

1186

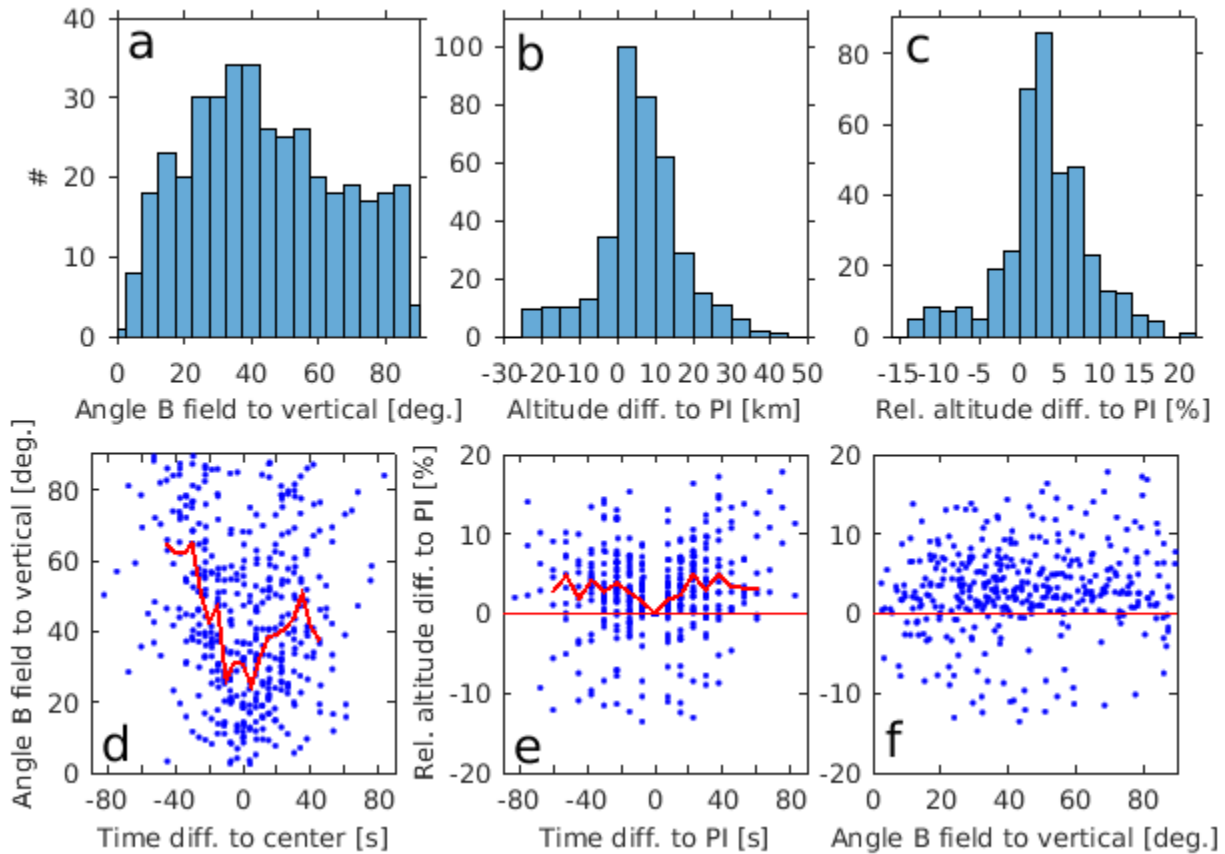


1187

1188 Figure 11: Maps showing regions of moderate crustal field strengths near the equator, in the  
 1189 Southern hemisphere (panel a) and Northern hemisphere (panel b). These are maps of the angle  
 1190 of the crustal magnetic field to the vertical from the model of Cain et al. (2003) evaluated at 150  
 1191 km altitude, represented as color coded contours from 15 to 75° per step of 15° (going from near  
 1192 horizontal to near vertical), using the colorbar on the left side. Fields of strength < 30 nT are  
 1193 ignored. The footprint of MEX at the times of available EDPs of the time series of the individual  
 1194 events observed in these regions are superposed onto the maps, colored for each event by the  
 1195 altitude differences between the PI EDP and the other EDPs relative to the altitude of the PI EDP

1196 (in %), all taken at a fixed frequency 1.936 MHz. Negative altitude differences are colored in  
 1197 blue, zero differences in white and positive differences in red, using the colorbar on the right  
 1198 side. The date and time of the PI EDP are written next to each event, and its location marked by a  
 1199 black 'x'.

1200

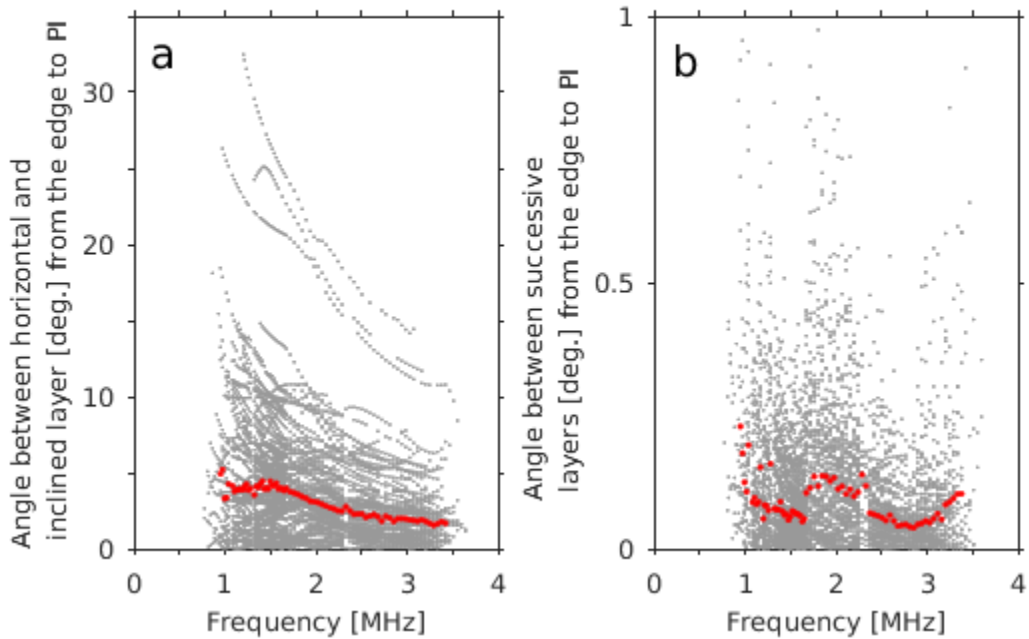


1201

1202 Figure 12: In this figure, the data points correspond to the altitude level at a fixed frequency  
 1203 1.936 MHz of all the available EDPs of the time series of all the events. (a) Distribution of the  
 1204 angle of the crustal magnetic field to the vertical. (b) Distribution of the altitude differences  
 1205 between the PI EDP and the other EDPs of the time series per event. (c) Distribution of the  
 1206 altitude differences between the PI EDP and the other EDPs of the time series, relative to the

1207 altitude of the PI EDP (in %), per event. (d) Superposed epoch analysis of the angle of the crustal  
1208 field to the vertical, using the time difference in seconds compared to the center time of the  
1209 density structure (which is centered at 0 s). Negative times are before the center time and  
1210 positive times are after. The red line indicates the median values as a function of superposed  
1211 epoch time. (e) Superposed epoch analysis of the relative altitude differences, using the time  
1212 difference in seconds compared to the PI EDP time (which is centered at 0 s). Negative times are  
1213 before the PI EDP time and positive times are after. The red line indicates the median values as a  
1214 function of superposed epoch time. (f) Scatter plot of the angle of the crustal field to the vertical  
1215 versus the relative altitude differences.

1216



1217

1218 Figure A1: (a) Distribution of the angle between the horizontal and the inclined layer from the  
1219 edge point to the PI point, versus frequency, for all the events, for both the beginning and end

1220 edges, plotted as grey dots. (b) Distribution of the angle between successive inclined layers (of  
1221 consecutive frequencies), versus frequency, for all the events, plotted as grey dots. In both  
1222 panels, the angles are shown in absolute value; the red dots indicate the median values versus  
1223 frequency.

1224

1225

1226

1227

1228